INSTRUMENTS AND METHODS OF INVESTIGATION

Talbot and Talbot–Lau X-ray interferometers

V V Lider

Contents

Abstract. **The operating principles and capabilities of X-ray grating interferometry are described using Talbot and Talbot–Lau interferometers as examples. Various types of diffraction gratings and methods for their production are described. Methods for collecting data in radiography and computed tomography, the origin of artifacts in X-ray images, and methods of suppressing them are considered. Particular attention is devoted to dark-field X-ray imaging and its application in medicine.**

Keywords: X-ray radiation, refraction, interference, diffraction grating, X-ray moiré, phase contrast, dark-field contrast

1. Introduction

From the very first studies by Roentgen, radiography has established itself as a unique research method in various fields of science, technology, and medicine. However, for a number of applications, particularly, for imaging of weakly absorbing objects, such as biological tissues, traditional absorption radiography is inefficient, since in such objects the absorption of X-ray radiation is extremely small. Note that, when passing through matter, the wave not only is absorbed but

V V Lider
Federal Scientific Research Center Crystallography and Photonics,
Russian Academy of Sciences,
Shubnikov Institute of Crystallography, Russian Academy of Sciences,
Leninskii prosp. 59, 119333 Moscow, Russian Federation
E-mail: vallider@yandex.ru

also changes its phase. The phase shift $\Delta\varphi$ of X-rays passed through a sample with thickness Δz depends on the decrement of the X-ray refraction coefficient δ and equals $(2\pi/\lambda)\,\delta\Delta z$, and the absorption β is related to the intensity attenuation: $\ln(I_0/I) = (4\pi/\lambda)\beta\Delta z$. Parameters δ and β that determine the X-ray refractive index n far from the absorption edges ($n = 1 - \delta + \mathrm{i}\beta$) are described by the formulae [1]

$$\delta = \frac{\rho\lambda^2 r_0 N_A Z}{2\pi A},\tag{1}$$

$$\beta = \frac{\mu\lambda}{4\pi},\tag{2}$$

where λ is the radiation wavelength, N_A is the Avogadro constant, r_0 is the classical electron radius, ρ is the material density, Z and A are the atomic number and atomic weight of the sample material, and μ is the linear absorption coefficient.

Estimates of δ and β for biological tissues showed [2] that $\delta \approx 10^{-6} - 10^{-8}$, which is nearly 1000 times greater than $\beta\,(10^{-9} - 10^{-11})$ for X-rays in the energy interval from 10 keV to 150 keV. Therefore, the differences in the X-ray phase shift for tissues with different densities are much greater than the differences in linear absorption coefficients. Hence, the phase contrast imaging can significantly enhance the X-ray sensitivity to small changes in objects with a small absorption coefficient weakly varying over the object, because, for this method, the variations in the refractive index decrement δ in the studied object are important.

Several methods of X-ray phase contrast visualization have been developed [3, 4]. They can be divided into interferometric methods [5, 6], free-space propagation methods [7, 8], diffraction-enhanced imaging [9, 10], and speckle-based visualization [11]. They differ in the character of the detected signal,

experimental setup, and requirements regarding the radiation used (especially its spatial coherence and monochromaticity). Although some of these methods give perfect results for specific problems [6, 8, 10], none of them has yet found wide application in medicine or industry, characteristic of which is the use of a laboratory X-ray source with a wide field of view (up to a few centimeters) and a fairly compact setup.

By using diffraction gratings as optical elements, one can solve the problems that to date have hampered wide use of phase contrast in X-ray radiography and tomography.

The first report about an experimental setup consisting of two linear transmission gratings appeared in 2003 [12]. Two years later, in 2005, the first phase-contrast images obtained using diffraction gratings were published [13, 14]. The authors of Ref. [15] reported the first use of grating interferometry in metrological applications, including the wavefront analysis. All these initial experiments were conducted using sources of synchrotron radiation (SR). The transition from synchrotron sources to laboratory X-ray equipment was implemented in 2006 [16]. In 2007, the first phase-contrast tomograms using an X-ray tube were obtained [17]. The extension of the range of obtained information by means of dark-field imaging (visualization of small-angle scattering) was implemented in 2008 [18].

A grating interferometer is mechanically robust, easily adjustable, and almost insensitive to mechanical drift. Its requirements concerning temporal and spatial coherence are moderate. A grating interferometer is largely achromatic and, therefore, can be efficiently used with X-ray sources having a wide spectral distribution. Since grating interferometry is particularly sensitive to small phase gradients, it is an ideal method for the investigation of soft tissues, as needed in medicine and biology, and the possibility of working with a common X-ray tube opens prospects for using grating interferometry in clinical examinations. Moreover, this is the only method allowing simultaneously realizing the triad of absorption, phase-contrast, and dark-field imaging (recall that, in dark-field visualization, the image contrast is formed by recording only the radiation scattered by the object under study).

The above features make grating interferometry superior among other phase contrast methods and lay the foundation for the wide use of phase-contrast X-ray radiography and tomography [19, 20].

2. Talbot interferometer

In 1836, Talbot [21] discovered that when a primary coherent wave passes through a periodic structure, e.g., a diffraction grating, a self-reproduction of its image occurs at distances $d_T = 2mp^2/\lambda$ (where p is the grating period, $m = 1, 2, 3, \ldots$). This phenomenon is called the 'Talbot effect' and the distance d_T is called the 'Talbot distance.' Later, the fractional Talbot effect was also discovered, i.e., for example, the self-imaging of a phase grating with period p could be observed at a distance of

$$d_m = \frac{(m-1/2)\, p^2}{4\lambda} \, . \tag{3}$$

For a grating of any type, it is convenient to present Eqn (3) as [22]

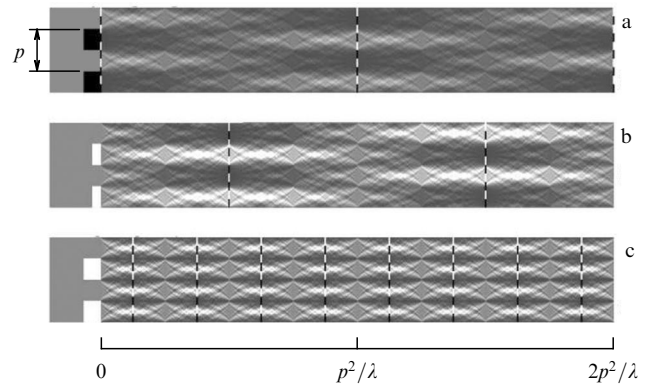$$d_m = \frac{mp^2}{2\eta^2 \lambda} \, . \tag{4}$$

Figure 1. Intensity distribution of an incident coherent plane wave behind a grating with period p. Patterns differ only in the grating optical properties: (a) amplitude grating with completely absorbing lines; (b) phase grating (zero absorption) with lines shifting the X-ray phase by $\pi/2$; (c) phase grating with lines shifting the X-ray phase by π. In all three figures, black-and-white dashed lines denote the points of maximum contrast [22].

Interference from a phase grating will always have a maximum contrast at odd orders ($m = 1, 3, 5, \ldots$), whereas an amplitude grating will always produce maximum contrast at even orders ($m = 0, 2, 4, \ldots$). The coefficient $\eta = 1$ for an amplitude grating or a phase grating with a phase shift equal to $\pi/2$, and $\eta = 2$ if the grating provides a phase shift of π. The difference among these three types of gratings (amplitude grating, quarter-wave grating, and half-wave grating) in terms of intensity distribution behind the grating is shown in Fig. 1.

The Talbot X-ray interferometer consists of two diffraction gratings G_1 and G_2 (Fig. 2). The G_1 grating with period p_1 acts as a beam splitter and causes a periodic modulation of the wave front. The period of the Fresnel interference pattern is about several microns and, as a rule, is much smaller than the detector resolution. Therefore, it is necessary to place in front of the detector a second grating G_2 with strongly absorbing lines, acting as an analyzer. The G_2 grating with period $p_2 = p_1/\eta$, made of a strongly X-ray-absorbing material, should be located in one of the planes of maximum contrast of the interference pattern [12, 13, 23, 24].

While the analyzer grating G_2 should be an amplitude grating, since it plays the role of a mask, the beam splitter grating G_1 can be a phase or absorption grating. It is desirable to use a phase grating, i.e., a grating with insignificant X-ray absorption. When using a phase grating, the optimal visibility (contrast) is improved when the grating material and thickness are chosen so that the phase shift of X-ray radiation passing through the grating equals $\pi/2$ or π. Note that for a plane coherent wave $p_2 = p_1$ (the phase shift being $\pi/2$) and $p_2 = p_1/2$ (the phase shift being π).

When superposing two linear gratings (in our case, these are the gratings G_1 and G_2), a moiré pattern arises [25–27].

The moiré pattern appears in the form of a linear periodic pattern with the period substantially larger than the period of each of the two structures. If the structures consist of a system of equally spaced planes, parallel to each other, with slightly differing interplanar spacings d_1 and d_2, then the moiré pattern arises with the period $\Lambda_d = d_1 d_2/|d_1 - d_2|$, called the dilatation moiré pattern. If systems of planes with similar periods d are rotated relative to each other by a small angle θ, then a rotation moiré pattern arises with the period $\Lambda_\theta = d/\theta$
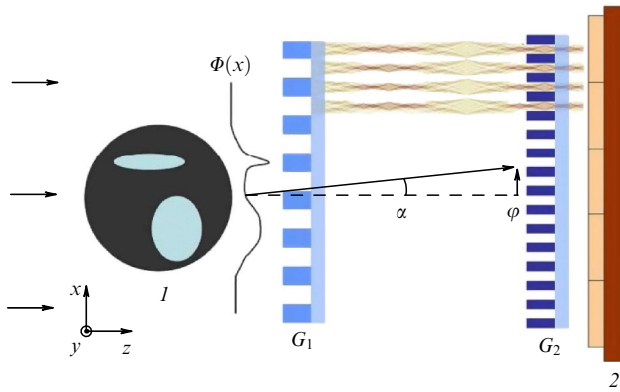
Figure 2. Schematic diagram of a Talbot interferometer using a parallel beam. Sample *1* in front of the phase grating distorts planar wavefront Φ and causes a lateral (in the *x* direction) shift of interference fringes at the grating G_2 location place (*2* — pixel detector) (see text) [28].

Figure 3. Schematic of rotation (a) and dilatation (b) moiré pattern formation.

[26, 27]. The fringes of the dilatation moiré pattern are parallel to the direction of the grating lines, while the fringes of the rotation moiré pattern are perpendicular to it (Fig. 3). In addition to the considered moiré pattern types, there is also a translation moiré pattern: when moving structures with $d_1 = d_2 = d$ and $\theta = 0$ with respect to each other in the direction normal to their lines, it is possible to record a periodic (sinusoidal with a period of *d*) variation in the transmitted radiation intensity [27]. Looking ahead, we note that the Talbot interferometer uses all three methods for obtaining a moiré pattern.

The object of study placed in front of the grating G_1 can cause a deviation in an X-ray from the initial trajectory by an angle of α (see Fig. 2). The angle α is proportional to the local gradient of the object phase variation $\partial\Phi/\partial x$ and can be quantitatively determined as [13]

$$\alpha(x,y) = \frac{\lambda}{2\pi}\frac{\partial\Phi(x,y)}{\partial x}, \tag{5}$$

where *x* is the axis perpendicular to the optical axis and the grating lines (see Fig. 2).

The beam refraction causes a shift of the interference pattern along the *x*-axis. This fringe shift measured in radians with respect to the period p_2 is expressed as

$$\varphi(x,y) = \frac{2\pi d\alpha(x,y)}{p_2} = \frac{\lambda d}{p_2}\frac{\partial\Phi(x,y)}{\partial x}. \tag{6}$$

Here, *d* is the distance between gratings G_1 and G_2.

Hence, measuring the change in the position of the interference pattern, we can get information on the phase change caused by the studied object [28].

From Eqn (6), it follows that the sensitivity of a Talbot interferometer linearly increases with distance *d* between the gratings. However, selecting a large *d* value results in a loss of spatial resolution.

When ignoring any dispersion in the sample, the limits of achromaticity are determined by a decrease in the interferometer efficiency due to the deviation in the X-ray photon energy from its design value. The half-width $\Delta\lambda = (\lambda_2 - \lambda_1)/2$ of the interval between wavelengths λ_1 and λ_2 (on both sides of the design wavelength λ_0), at which the interference pattern contrast passes through zero, can be taken for the energy range in which the interferometer efficiently operates. The authors of Ref. [13] showed that $\Delta\lambda = \lambda_0/(2m-1)$. Thus, the
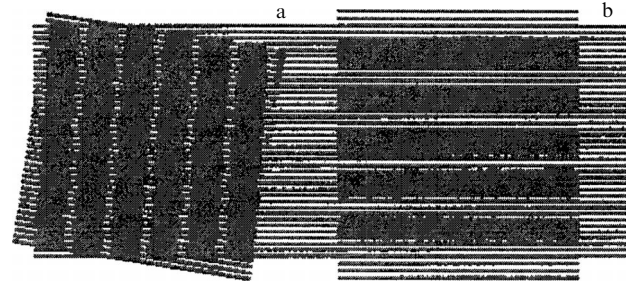
higher the order *m* of the Talbot distance used, the more rigorous the monochromaticity requirements. Nevertheless, even for a Talbot distance of the 5th order, the acceptable bandwidth $\Delta\lambda/\lambda_0$ is more than 10%. It was theoretically shown that the image obtained using X-ray radiation with the bandwidth $\Delta\lambda/\lambda_0 = 1/8$ is almost comparable to the image obtained with monochromatic X-ray radiation [29]. Numerical modeling [30] has shown that the image visibility is weakly sensitive to the polychromaticity and, therefore, it is possible to use the Talbot interferometer in combination with polychromatic X-ray sources, which was experimentally confirmed [31].

3. Talbot–Lau interferometer

To improve the magnified image of a sample and to increase the interferometer field of view, a conical beam is used (see Fig. 4) [32, 33].

The self-reproduction effect arises when coherent X-ray radiation illuminates a phase grating whose period is smaller than the transverse coherence length l_{coh}, i.e., $l_{\mathrm{coh}} = (L/w)\lambda \geqslant p$ (*w* is the source size, *L* is the distance between the source and the grating). This is the coherence condition for a Talbot interferometer [24, 34, 35].

Most often, synchrotron radiation sources and microfocus X-ray tubes satisfy the coherence condition, but this is not so for usual X-ray tubes. In the latter case, to obtain a phase contrast image in front of the source, it is necessary to install an absorption grating G_0 (Fig. 4), and its period p_0 should be small enough to provide the generation of partially coherent X-ray radiation. Such a framework consisting of three gratings is called a Talbot–Lau interferometer, in which the role of grating G_0 is to create a number of individually coherent but mutually incoherent subsources.

In the case of a conical beam, the Talbot distances $d_m = (m/2\lambda)(p_1/\eta)^2$ for a plane wave will be rescaled to a spherical wave [36]:

$$d_m^* = \frac{L d_m}{L - d_m}, \tag{7}$$

where *L* is the distance between the X-ray source and the grating G_1 (in Fig. 4, $L = l + s$ and $d_m^* = d$). Since the source mask G_0 can comprise a large number of individual apertures, each of them creating a fairly coherent virtual line source, standard generators of X-ray radiation with a source size of more than a square millimeter can be efficiently used. In order for each line source created by the G_0 grating to make a constructive contribution to the image formation process, the setup geometry must satisfy the condition $p_2 = (p_1/\eta)(1 + d_m^*/L)$, $p_0 = L p_2/d_m^*$ [16, 22, 37].
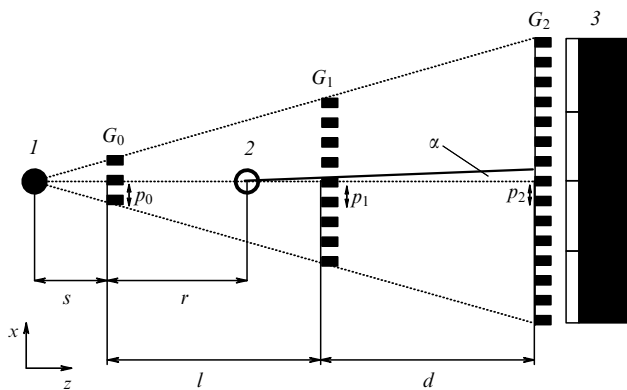
Figure 4. Schematic diagram of a Talbot interferometer using a conical X-ray beam: *1* is the source of X-ray radiation, *2* is the sample. There are three gratings, G_0, G_1, G_2, with periods p_0, p_1, and p_2, respectively, behind which detector *3* is placed. Grating G_0 is located at distance s from the source, and the sample, at distance r from the grating [39].

The angular sensitivity [38, 39] and the spatial resolution are two key determining characteristics that need to be optimized in a Talbot–Lau interferometer.

The minimum attainable effective size of the system pixel σ_{eff} is limited by the focal spot size τ of the source and the detector pixel size σ and equals [33]

$$\sigma_{\text{eff}} = \frac{\tau\sigma}{\tau + \sigma} \, . \tag{8}$$

Depending on the detector system, the spatial resolution Δ is determined by the inequality $\Delta \geqslant \sigma_{\text{eff}}$ [40].

The interferometer sensitivity can be quantitatively estimated by the minimum detectable refraction angle α_{min}, which is proportional to the minimum detectable electron density variation in the sample. The angle α_{min} directly depends on the signal-to-noise ratio of X-ray patterns and mathematical algorithms [41] used for image reconstruction.

The angular sensitivity has a geometric component determined by the choice of the grating period and the geometry of the X-ray interferometer. On the other hand, it is related to the total number of photons N detected in the course of image formation, mainly determined by the exposure time and the efficiency of X-ray radiation detection, as well as by the image visibility. The visibility V [13, 38] is defined as

$$V = \frac{I_{\text{max}} - I_{\text{min}}}{I_{\text{max}} + I_{\text{min}}} \, , \tag{9}$$

where I_{max} and I_{min} are the maximum and minimum intensities detected by the detector pixel. Because of the polychromaticity [38, 42] of laboratory sources and the usually limited absorption of X-ray radiation by gratings G_0 and G_2, the imparted 'visibility of method' in laboratory systems varies from 10 to 30% [43, 44].

The angular sensitivity formula in the case of a sample placed in front of grating G_1 has the form [39, 45]

$$\alpha_{\text{min}} = \frac{p_2}{\pi d} \frac{l + s}{r + s} \, N^{1/2} V \, . \tag{10}$$

Here, l and d are the distances between gratings G_0 and G_1, G_1 and G_2, respectively, s is the distance between the X-ray source and grating G_0, and r is the distance between grating G_0 and the studied sample.

Thus, the closer the sample to the G_1 grating, the smaller the refractive angles that can be detected [46].

From Eqn (10), it obviously follows that a greater distance d between the gratings and the smaller grating period p_2 will lead to higher angular sensitivity. Nevertheless, the distance d between the gratings and the period p_2 of the grating G_2 should be chosen in correspondence with the distances at which the Talbot fringes appear. It was shown in [45] that higher angular sensitivity when using gratings with a smaller period requires high-order Talbot geometry to compensate for the decrease in the propagation distance $r + s$.

For a given period of the phase grating p_1, when $l = d$ (see Fig. 4), the interferometer has the minimum possible total length $4d_m$. In addition, the absorbing gratings G_0 and G_2 have the same period ($p_0 = p_2$), which allows minimizing the cost of their manufacturing. As was pointed out above, for π-phase shift $p_1 = p_2$, therefore, $p_0 = p_1 = p_2$.

However, some applications, such as laboratory microtomography, require the object to be close to the source, e.g., for reducing the effective pixel size [45]. This requirement is satisfied using the so-called inverse geometry of the interferometer, for which $l < d$, i.e., the phase grating is closer to source grating G_0 than to the analyzer grating. The inverse interferometer geometry, according to the opinion of the authors of Ref. [46], provides the same sensitivity as the symmetric geometry, but at the same time reduces the requirements regarding the interferometer.

As a rule, the moving part of a tomographic system (gantry) requires enough space. Therefore, it is more profitable to place the sample at that side of the phase grating, where there is more room, i.e., between grating G_0 and phase grating G_1 for symmetric geometry and behind the phase grating for the inverse geometry. When the sample is placed behind the phase grating, Eqn (10) can be rewritten as [47]

$$\alpha_{\text{min}} = \frac{p_2}{2^{1/2} \pi L_{\text{g}} V N^{1/2}} \, , \tag{11}$$

where L_{g} is the distance between the sample and grating G_2.

4. Diffraction gratings

4.1 Manufacturing
Diffraction gratings [48] with periods in the micrometer range are basic elements of an interferometer (Fig. 5). Phase gratings are comparatively easy to manufacture; absorbing gratings for the corresponding X-ray radiation energies are more difficult to make, since they require lamellas with high attenuation at small periods.

The main parameters of X-ray diffraction gratings are the manufacturing material, the period p, the structure height h, and the slit size w. For X-ray interferometric visualization, the manufacturing of silicon microgratings requires precise vertical profiles, large aspect ratios A ($A = h/p$), high accuracy of period size p, large duty cycle v ($v = w/p$), uniformity over a large area, and, finally, the possibility of filling the silicon template with a material that highly absorbs X-ray radiation [49, 50], such as gold [51].

The main technical problem is to manufacture absorbing gratings. Especially for the mode of hard X-ray radiation (with tube accelerating voltage exceeding 60 kV), which is important for clinical applications, structures with a very high aspect ratio are needed. Since typical grating periods are in the range of 2–40 μm, and for acceptable efficiency the desirable
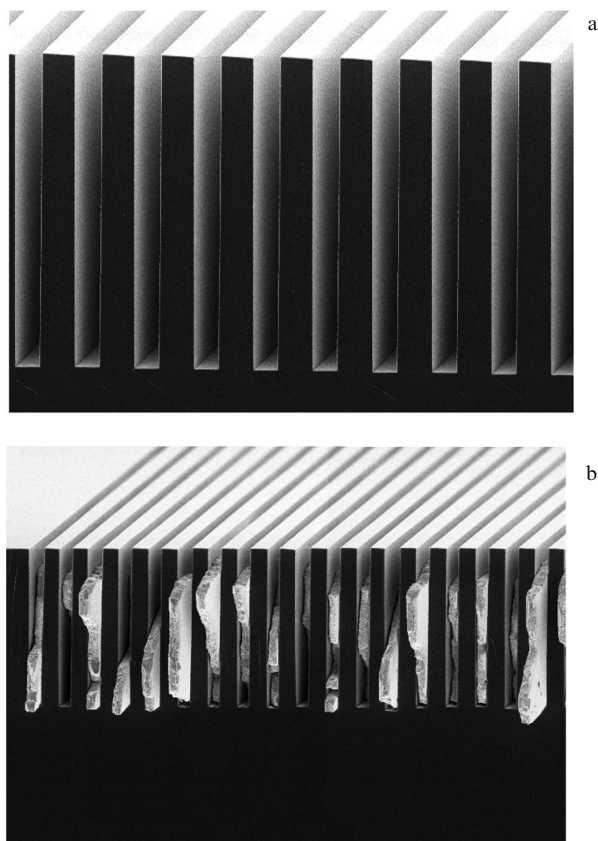
Figure 5. Scanning electron microphotographs of cross sections of interferometer gratings: (a) silicon grating of a beam splitter with a period of 4 µm and structures 22 µm high; (b) analyzer grating with a period of 2 µm, consisting of a silicon grating filled with gold [24].

Figure 6. Transmission grating structure: *1* — echelette substrate of Si, *2* — micrograting, *3* — upper layer of Si [64].

absorber height is up to a few hundred µm, only a few methods of grating production can solve this problem [52–54].

The key problem consists in precisely manufacturing the binary grating profile with exactly perpendicular sidewalls, which then can be filled by means of electrodeposition of other methods of metallization. The required grating structure can be obtained by deep X-ray lithography [55–57] or various methods of silicon anisotropic etching [58, 59]. When using deep reactive-ion etching, a precisely controlled alternation of etching and sidewall passivation stages is required to achieve strong etch anisotropy [59]. Notably, the profile has a tendency of changing with the etch depth [59]. As an alternative, gratings with high A in silicon can be implemented by anisotropic liquid etching of (110) silicon substrates with potassium hydroxide (KOH) or tetramethylammonium hydroxide (TMAH) using different etching rates along crystallographic planes, which yields perfect vertical side walls [58]. Chemical etching using a metal is becoming a new method, which provides a huge aspect ratio [60].

Filling with an absorbing material can be implemented by electrodeposition [58]. Other methods of metallization, such as atomic layer deposition [43], microinjection molding [61, 62], or hot stamping [49, 50], facilitate an increase in A and could possibly make the manufacturing process simpler and more economically efficient. When manufacturing gratings based on the LIGA (LIthographie, Galvanoformung, Abformung) process, a very high aspect ratio can be achieved [55, 63].

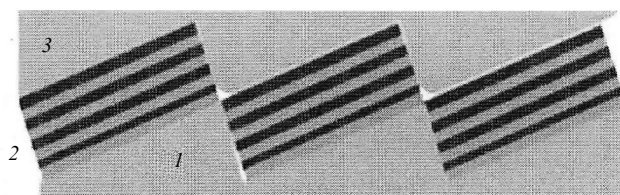The authors of Ref. [64] proposed a method of producing transmission gratings with a submicron period and centi-meter size by means of multilayer coating of a stair-shaped substrate (echelette). The advantage of this approach is the high aspect ratio of the multilayer coating and the large substrate area. Several layers are deposited on the horizontal surfaces of the 'staircase' by magnetron sputtering in a single run. The structure consists of alternating materials with different absorption coefficients. Each step forms a micrograting with the thickness equal to the step height, and the array of microgratings is an integral large-area grating with the continuity conditions taken into account (Fig. 6). In this case, the grating period can potentially be less than 100 nm.

The entire echelette is an array of microgratings covering a large area. The key moment worth noting here is that the thickness of the double layer is the grating period.

Reference [65] describes a multilayer echelette grating with a period of 200 nm, an aspect ratio of up to 200, and an area of 20 mm × 20 mm.

4.2 Optimization
Modern grating interferometers often use planar gratings, which always favor the use of parallel beam imaging geometries. An X-ray tube is usually a point source that emits a diverging X-ray cone-shaped beam. In this case, imaging with a plane grating has limitations in terms of both the field of view and the flux. The X-rays penetrating the grating structures at angles close to or greater than w/h do not participate in the formation of the interference pattern because of the shielding effect, which reduces the field of view. A possible solution to this problem is to manufacture cylindrically curved gratings, whose central curvature axis intersects with the focal spot of the source (Fig. 7a).

Using cylindrical gratings allows normal X-ray incidence, which leads to higher visibility in a wider field of view than in a common interferometer with planar gratings [40, 66–69].

Reference [66] describes curved gratings on a more flexible substrate, manufactured using a modified LIGA process [71]. Since usually silicon plates (200–500 µm thick) are rather fragile and can be bent only to a radius of a few tens of centimeters, the process was adapted for producing gratings on titanium substrates. Thanks to the small substrate thickness that amounts to only 50 µm, the substrate is very flexible and allows a curvature radius of a few centimeters without damaging the grating. More specifically, for a Talbot–Lau interferometer, the curvature radius of the initial grating G_0 should not be large in order to support the system geometry.

If the aspect ratio is too large, the grating structures have a tendency to collapse or deform (e.g., due to capillary forces). Moreover, when using a broadband source, photons with an energy beyond the design value must also be efficiently blocked by the gratings, which requires an even larger aspect ratio.
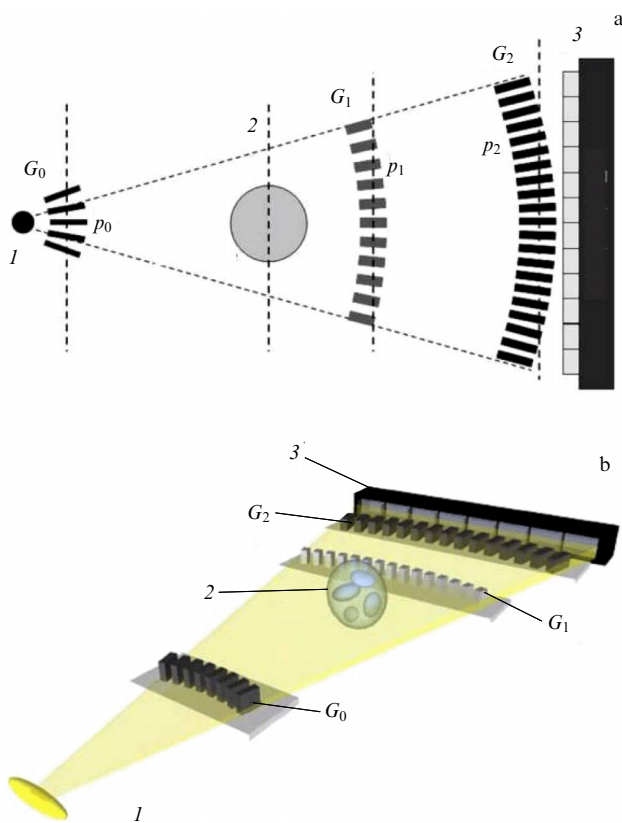
Figure 7. Schematic diagrams of a Talbot–Lau interferometer with curved gratings (*1* — radiation source, *2* — sample, *3* — detector): (a) direct illumination mode [40]; (b) side illumination mode. $E = 100$ keV, distance between the source and grating G_0 is 23 cm, distance between gratings G_0 and G_1 and gratings G_1 and G_2 is 16 cm [70].

The design proposed by the authors of Ref. [70] is based on the so-called side illumination of the interferometer. Upon side illumination (Fig. 7b), the effective height of the grating structure is determined by the grating size along its lines, which, in essence, allows an arbitrarily large aspect ratio. The combination of side illumination with curved gratings allows obtaining phase contrast images at arbitrary design energies and with a maximum field of view in the diffraction plane.

A two-dimensional X-ray image can be obtained by scanning a sample or a narrow fan beam. It was demonstrated that the scanning method provides a lower radiation dose than the traditional approach based on illuminating a large area, which is important for using a grating interferometer in medicine.

Alongside the aspect ratio, the duty cycle is an important parameter for setup optimization and achieving the best visibility for a given set of specifications. The duty cycle value of $v = 0.5$ (in Ref. [72], a more exact value of $v = 0.55$ is presented) is considered optimal for Talbot interferometer gratings. However, in Ref. [73] by means of modeling and appropriate experiments, it was shown that a Talbot–Lau standard-type apparatus with an duty cycle 0.5 for grating G_1 is not always the best choice. With an increase in the duty cycle of any grating, as follows from Eqns (10), (11), the total number of detected photons increases, but the angular sensitivity decreases. Therefore, according to the authors of Ref. [47], there are optimal duty cycles for obtaining more

sensitive phase contrast images. Their optimal values are 0.3815 (G_0), 0.3766 (G_1), and 0.3788 (G_2).

As was mentioned above, the difficulty of manufacturing the analyzer grating is one of the main obstacles to applications of differential phase contrast imaging. To record an X-ray interferogram, the authors of Refs [74–77] proposed a new X-ray scintillation screen with functions of an analyzer grating. The structured scintillator acts as a usual scintillator and as an analyzer grating. To allow its operation as an analyzer grating, half of the period of the structured scintillator is filled with a material sensitive to X-ray radiation, such as cesium iodide doped with Tl (CsI:Tl), which converts X-ray radiation into visible light. The other half-period of the structured scintillator is made of silicon. As compared to an absorbing grating of gold, the structured scintillator is more suitable for broadband X-ray radiation, especially for obtaining X-ray phase-contrast images with a higher energy of photons.

The disadvantage of using the initial grating G_0 is that more than half of the X-ray flux is wasted, which, in turn, significantly reduces imaging efficiency. To increase the interferometer sensitivity, it is necessary to use gratings G_0 with small periods of only a few micrometers [38]. In turn, to provide sufficient absorption of the X-ray radiation, the line thickness of grating G_0 should reach several ten micrometers with a high aspect ratio, which is very difficult to achieve technically.

Several methods aimed at avoiding the use of grating G_0 and related limitations have been proposed. One of the methods implies producing grooves on a rotating anode [76, 78], but this approach limits the interferometer in terms of the field of view, since the coherence is different at different positions of the target. Shimura et al. [79] successfully demonstrated how it is possible to use efficiently a microstructured array anode target (MAAT) to construct a compact Talbot–Lau interferometer. The results of two-dimensional visualization with a rather low spatial resolution and at a low operating energy (20 keV) were obtained. Morimoto et al. [80] experimentally demonstrated a compact Talbot–Lau interferometer with a MAAT source. However, its power (60 W) and operating energy (20 keV) are too small for rapid imaging of a large sample.

The new source of X-ray radiation with a structured anode microarray [81] has a few advantages as compared to the traditional combination of a large-size X-ray radiation source with an absorbing grating, including a large flux of X-ray quanta and a large field of view, and these advantages become noticeable for the X-ray radiation energy above 30 keV. The MAAT source of X-ray radiation comprises an anode, consisting of microstructured metallic inserts in diamond, which affect the X-ray emitters by creating a periodic array of micron-size subsources without an absorbing grating. The tungsten-based MAAT pattern with an area of 0.4×0.4 mm^2 was embedded in a polycrystalline diamond substrate 10 mm in diameter and 1 mm thick. The transmission target is formed using traditional processes of photolithography and reactive-ion etching The pattern period is 3.0 μm, and the duty cycle is 0.33, which yields tungsten lines 1.0 μm thick separated by strips of diamond 2.0 μm thick [82].

To conclude, we note that the optimal absorbing grating, according to the authors of Ref. [83], exists only in the sense of Pareto optimality, i.e., one of the system parameters cannot be improved without worsening some other parameter.

Therefore, it is necessary to specify the relative importance of various contrasts (absorption, phase, and dark-field) before designing the structure of the absorption grating. There is an unavoidable compromise between the imaging qualities of these contrasts, even if the gratings are manufactured perfectly. Moreover, this compromise changes upon varying the experimental parameters, which complicates the comparison of different devices in efficiency. When optimizing an absorption grating to improve the visibility, the absorption contrast will unavoidably suffer, thus changing the balance between the three contrasts and displacing their comparison in favor of the differential phase contrast and the dark-field contrast.

5. Methods of extracting information

Coherent X-ray radiation of a source penetrates through an object (installed on the optical path) and the first phase grating, creating an interference pattern. Then, the radiation partially absorbed by the amplitude grating forms a detectable moiré pattern on a detector. It is well known that the detected interference pattern encodes three physical parameters of the scanned object. The first is the absorption index of the object. It can be determined by measuring a decrease in intensity of the recorded X-ray. The second parameter is the differential phase. The phase of incident X-ray differentially changes when passing through the object. As a result, the pattern of fringes distorts. This parameter is attractive, because it allows imaging soft matter, unobservable in absorption images. The third parameter is the small-angle scattering of X-rays. The coherence of the incident X-rays is reduced, which is determined by the object microstructure. Thus, it is possible to detect microstructure features by degradation of the pattern of fringes. All parameters are extracted from the observed pattern of fringes using the demodulation process. Currently, the phase demodulation methods used in grating interferometry can be conventionally divided into two types: the phase-stepping method and the Fourier transform [84, 85].

The Talbot interferometer is successfully used not only for phase image formation but also as a wave front sensor, which is one of the elements of the metrology system. The analysis of moiré fringe distortion allows characterizing wavefront aberrations of the order of a wavelength [86, 87].

5.1 Phase-stepping method

The main purpose of the method is to estimate local changes in the radiation intensity $I(m, n, x_g)$ caused by the object, and, based on a few measurements, to construct images, including a dark-field image [18, 52, 88, 89]. Under a stepwise displacement of one of the gratings in the direction x_g, perpendicular to the grating lines, the intensity signal $I(m, n)$ in each pixel m, n in the detector plane follows a sinusoidal curve (the so-called phase-stepping curve) (Fig. 8). Only a finite number of N_{gs} steps are executed during the period p_2. Then, the recorded intensity $I_k(m, n)$ for step $k = N_{gs} x_g / p_2$ can be written in the form of a Fourier series:

$$I_k(m,n) = \sum_i a_i(m,n) \sin\left(\frac{2\pi i k}{N_{gs}} + \phi_i(m,n)\right)$$

$$\approx a_0(m,n) + a_1(m,n) \sin\left(\frac{2\pi k}{N_{gs}} + \phi_1(m,n)\right), \quad (12)$$
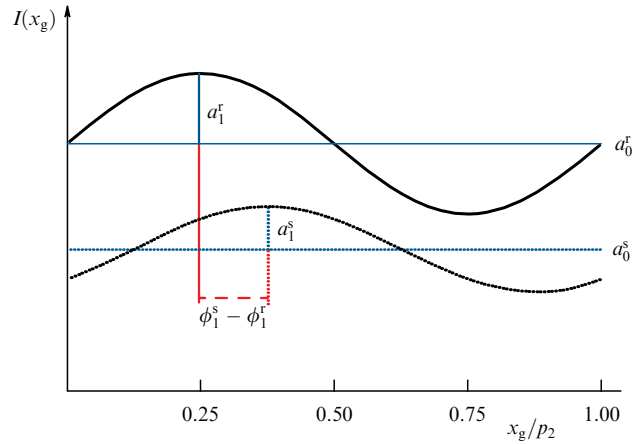

Figure 8. Measured intensity in a pixel of a detector for the etalon (superscript r) and scanning with a sample (superscript s) in one cycle of phase-stepping method [90].

where a_i are the amplitude coefficients, ϕ_i are the corresponding phases, and p_2 is the period of grating G_2. The coefficients a_0, a_1, and ϕ_1 are extracted from the obtained data set I_k ($k = 1 \ldots N_{gs}$) of the phase-stepping curve by means of the fast Fourier transform [13, 18] and are used to calculate the three images. For this purpose, no fewer than three measurements are needed ($N_{ps} \geqslant 3$); typically, the number of measurements lies in the range of 5–11 [18]. Then, the normalized mean transmission coefficient of the sample in each pixel of the detector is determined as

$$T(m,n) = \frac{a_0^s(m,n)}{a_0^r(m,n)}, \quad (13)$$

where the superscripts s and r denote values measured with and without the sample in the X-ray beam, respectively. In addition, as was shown earlier [16], the differential phase contrast images $DP(m, n)$ can be obtained by analyzing the lateral shift of the intensity modulation, i.e., the value of $\phi_1(m, n)$ in Eqn (12):

$$DP(m,n) = \frac{\phi_1^s(m,n) - \phi_1^r(m,n)}{2\pi}. \quad (14)$$

Finally, if we determine the visibility of the phase-stepping curve as $v^i(m, n) = a_1^i / a_0^i$ ($i = $ r or s), then the visibility of a dark-field image V will be

$$V(m,n) = \frac{v^s(m,n)}{v^r(m,n)} = \frac{a_1^s(m,n)\, a_0^r(m,n)}{a_0^s(m,n)\, a_1^r(m,n)}. \quad (15)$$

For homogeneous samples, i.e., those with a negligibly small contribution of small-angle X-ray scattering, the value of visibility remains unchanged, and $V(m, n) = 1$. However, a sample characterized, for example, by strong density fluctuations and, therefore, large signals of small-angle scattering, demonstrates a significant visibility decrease, $V < 1$ [91].

Figure 9 presents X-ray images of a living mouse. A usual radiograph (Fig. 9a) shows a very good contrast between the bones and soft tissues, mainly due to the increased attenuation of X-ray radiation by calcium as compared to lighter elements of organic molecules. The differential phase contrast image (Fig. 9b) enhances the specification of soft tissues. Notably, distinctly shown are the boundaries of air-filled areas such as the trachea (marked with an arrow) or lungs.
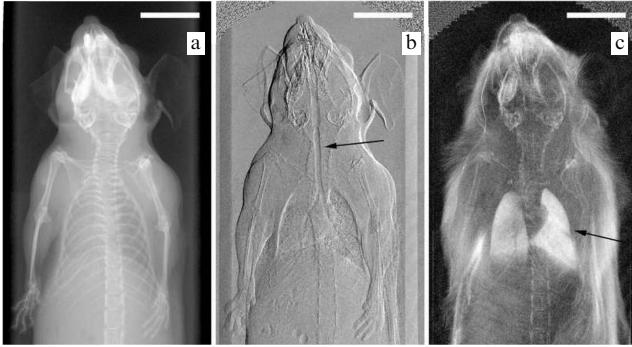
Figure 9. First multi-contrast X-ray images of a mouse *in vivo*: (a) common absorption-based X-ray image; (b) differential phase contrast image based on X-ray refraction; (c) dark-field image based on X-ray scattering. Arrows mark examples of increased contrast regions: refraction of X-ray by the trachea (b) and scattering by fur and lungs (c). White scale bars correspond to 1 cm [92].

Figure 10. Common (a) and stepped (b) structure of grating G_2 [97].

Finally, the dark-field image (Fig. 9c) due to the small-angle scattering of X-rays enhances the details containing microstructures of a subpixel size, such as fur and the lungs. In particular, the lungs demonstrate a strong signal, since their main morphological structures, the alveoli, have a typical size of a few ten micrometers [92].

5.2 Phase-stepping method optimization
The phase-stepping method implies moving one of the gratings stepwise several times during a period; the data acquisition is performed when it is in a static position. Therefore, the data acquisition slows due to the time of grating movement, which increases the dose of the studied object radiation. The integrating-bucket (IB) technique [93] can decrease the sample radiation dose and improve the rate of data acquisition by moving the grating continuously [94]. During one period divided into sections, the data acquisition is performed continuously while the grating is within a definite section. In this case, the total scanning time and the time of data acquisition by the detector are equal.

However, it should be noted that the described method implies movement of the grating. It is clear that a method that would allow extracting phase information without the necessity of moving the grating would be a breakthrough, ensuring fast high-sensitivity phase contrast X-ray imaging of a sample at a low radiation dose.

The back-projection method is an alternative method of phase reconstruction [19]. In this approach, a sinusoidal phase-stepping curve is approximated by a linear function in the region of the maximum derivative. The method uses antisymmetric shooting: upon rotation of the sample by 180°, the X-ray absorption remains unchanged, but the phase changes sign. Information on both the phase and the absorption can be extracted by an appropriate combination of back-projection images instead of collecting three or more projection images, as is required by the phase-stepping method. Thus, instead of performing full phase stepwise scanning, only two projections in the chosen grating positions are recorded. This method has been extended for operating with two-dimensional gratings [95] and for the geometry of a fan (conical) beam [67].

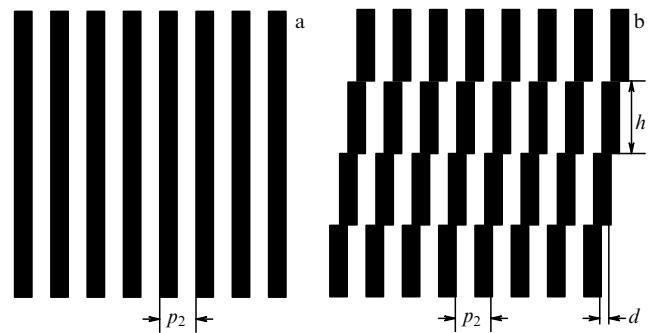The linear region of the sinusoidal phase-stepping curve is most sensitive to phase shifts. In contrast, the region of the phase-stepping curve extrema is sensitive only to the changes in the curve amplitude, i.e., the dark-field signal. This means that, in the phase stepping approach, only half of measured points contribute to the phase information, whereas the other half determines the dark-field signal. The back-projection method uses only those points in the linear region which make the maximum contribution to the phase signal. In this case, the information on the dark-field signal is absent.

The authors of Ref. [96] proposed a theoretical justification for a visualization method called angular signal radiography, based on collecting data at four points of the phase sinusoid: the minimum, the ascending slope, the maximum, and the descending slope. In Ref. [97], the possibility of realizing a method of angular signal radiography by means of an alternative construction of the stepped absorption grating [98] was considered. The grating (Fig. 10) is divided into individual lines, each having a height h equal to the height of a detector pixel. Any two adjacent rows of the grating have relative displacement d, equal to $(1/M)p_2$ (M is the number of 'steps', p_2 is the interference pattern period).

Such a grating allows reconstructing 'three contrasts' from only one projection image. Thus, all components of the interferometer, including the gratings, the detector, the X-ray source, and the sample, stay immobile.

Later, by analogy with stepped grating, an absorption grating comprising a set of groups of linear Si/Au structures has been specially developed. Each group is embedded in the grating with displacement d, and the linear structures have period p_2 within each group [99].

5.3 Fourier transform method
However, the phase-stepping method has a number of substantial drawbacks. For example, multiple mechanical movements of a grating can generate a vibration, negatively affecting the interferometer stability, and the low rate of data acquisition because of the complexity of the phase step procedure increases the radiation load on the object of study, which negatively affects the possibility of using the method in medicine.

To avoid the phase step procedure during data acquisition, a method using a single image of moiré fringes, called the Fourier transform of a moiré pattern, has been proposed as an alternative [12, 31, 100–105]. To implement the method, the carrier moiré rotation bands are introduced into the image by rotating grating G_2 relative to grating G_1 around the optical axis by an angle θ (Fig. 11). However, the spatial resolution is in principle limited by the separation between
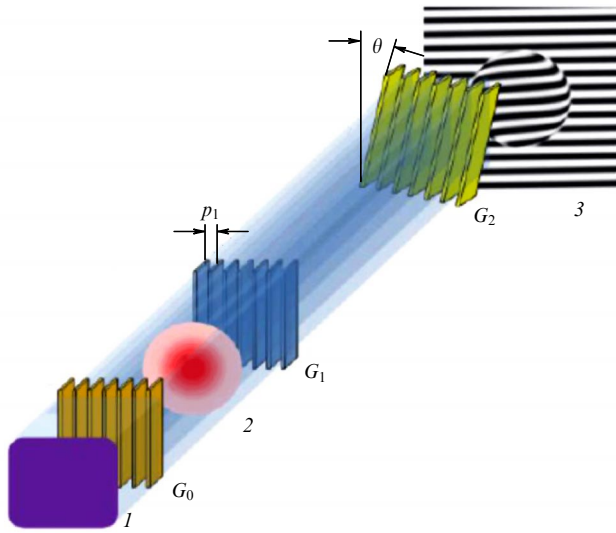
Figure 11. Schematic diagram of a Talbot–Lau interferometer for implementing the Fourier transform method: 1 — X-ray source, 2 — sample; to create moiré pattern 3 in the detector plane, grating G_2 is rotated relative to grating G_1 by the angle θ [105].

carrier fringes. Therefore, for better spatial resolution, finer carrier fringes are preferable, which can be obtained by increasing θ, although the generation of more perfect rotation moiré fringes may have a disadvantage consisting in the loss of their visibility [101].

It is desirable to have a moiré pattern with a period close to a triple detector step. This allows maximum separation of peaks of harmonics in the Fourier space [12, 31].

The moiré pattern of intensity $I(x, y)$ on a detector pixel (x, y) can be described by means of the first two terms in the Fourier expansion:

$$I(x, y) \approx a_0 + a_1 \cos \left[\frac{2\pi}{p_{\mathrm{m}}} (x \cos \theta + y \sin \theta) + \phi \right], \quad (16)$$

where x and y are the coordinates in the detector plane, a_n is the nth Fourier coefficient, p_{m} is the period of the rotation moiré pattern, and ϕ is the phase. Executing the 2D Fourier transform [100] leads to the representation of the image

$I^*(x, y)$ in the Fourier space. Projection images of each of the three contrast mechanisms are extracted by performing an inverse Fourier transform in the subdomains $I^*(x, y)$ [102, 104].

5.4 Wavefront sensor

To optimize systems of adaptive and active optics, exact information on the wavefront of the X-ray focused beam is needed. Therefore, before correcting the wavefront phase, it is necessary to measure it.

The metrology of optics *in situ* is a noncontact high-accuracy system of online testing. It is shown in [86, 87, 106–112] that a Talbot interferometer can be used to measure the parameters of reflecting optical surfaces, such as deformable mirrors, bimorph mirrors (Fig. 12a), multilayer mirrors, and refractive X-ray lenses.

The curvature radius of the X-ray radiation wavefront and its distortions can be measured using a single image [108]. When rotating the absorbing grating by an angle α and the phase grating by an angle β around the optical axis, a rotational moiré pattern is formed in the detector plane (Fig. 12b).

The tilt angle ϑ of moiré fringes (Fig. 12b) can be expressed as [113]

$$\tan \vartheta = \frac{\cos \alpha - \kappa \cos \beta}{\sin \alpha - \kappa \sin \beta}, \quad (17)$$

where κ is the coefficient of reduction, determining the ratio of periods of the absorption grating and the moiré pattern. The periods x and y of fringes along the detector axes d_x and d_y are expressed as

$$d_x = \frac{d_2}{\sin \alpha - \kappa \sin \beta}, \quad (18)$$

$$d_y = \frac{d_2}{\cos \alpha - \kappa \cos \beta}. \quad (19)$$

From the system of Eqns (18), (19), it is possible to extract the parameters κ and α, using two images obtained at different tilt angles β of the phase grating.

From the given pattern of moiré fringes, the local wavefront curvature radius R can be determined using the
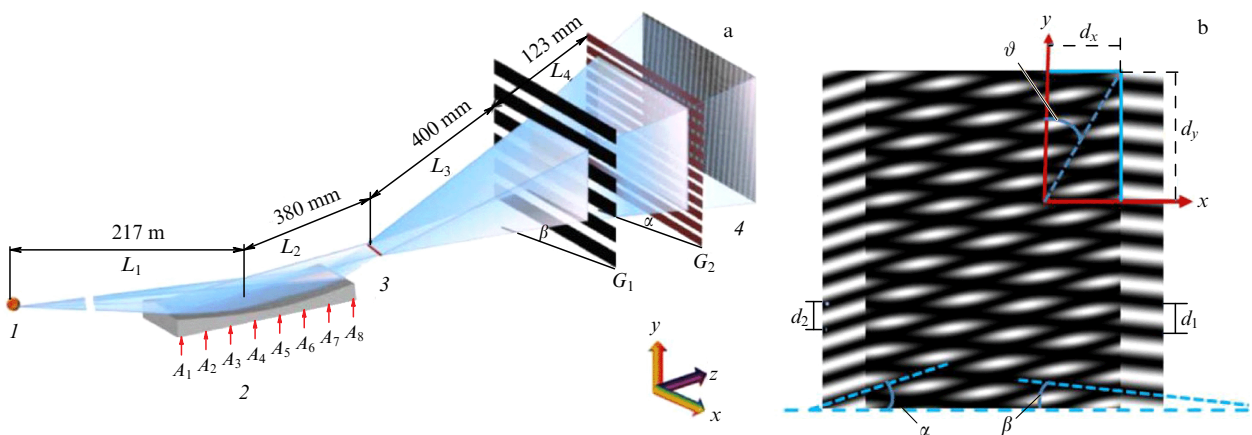

Figure 12. (a) Optical system for optimizing the bimorph focusing mirror with 8 piezoelectric actuators $A_1, A_2, \ldots, A_8$ using a Talbot interferometer (1 — X-ray source, 3 — focus formed by the mirror 2, 4 — detector) [108]; (b) formation of moiré fringes, which have tilt angle ϑ relative to the vertical axis, when the tilt angles of gratings G_1 and G_2 relative to the horizontal axis equal β and α, respectively [86].

equation [86, 112]

$$R(y) = \frac{d_m^* \tau \kappa(y)}{2 - \tau \kappa(y)}, \qquad (20)$$

where $\tau = p_2/p_1$, and d_m^* is given by Eqn (7).

Finally, the wavefront tilt angle S_y can be reconstructed by integrating the reciprocal of the curvature radius R^{-1} along the vertical direction y [113]:

$$S_y = \int R^{-1}(y)\, \mathrm{d}y. \qquad (21)$$

6. Two-dimensional interferometer

The one-dimensionality of optical elements and the information on the direction represented by them can give rise to various problems, especially in phase and dark-field images. These problems can be overcome by simultaneous access to the information in two perpendicular directions in the image plane.

Two approaches to recording the full vector of the wavefront gradient using a grating interferometer have been reported. One of them is to rotate the sample or the entire interferometer around the optical axis by 90° [114, 115]; however, such a method requires the presence of an additional rotation axis and, therefore, a complication of the interferometer design. Another option is to use 2D grating structures [116–118]. However, in this case, the data acquisition is slow, since it requires stepwise phase scanning in two dimensions, or, when using the Fourier transform mode, worsens the spatial resolution [119].

The operational distances in a two-dimensional grating interferometer are the same as in the one-dimensional version. The grid image, produced by grating G_1, is analyzed by means of two-dimensional phase stepwise scanning by moving one of two optical elements in the plane, perpendicular to the optical axis. The intensity distribution measured in the course of scanning can be analyzed by means of the two-dimensional Fourier transform. The information arriving from two orthogonal directions can be combined to improve the quality of dark-field and phase images [120].

The two-dimensional grating interferometer removes most of the general reconstruction artifacts that usually appear when using a 1D interferometer.
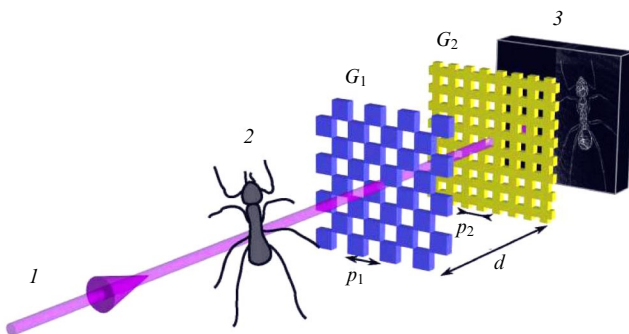

Figure 13. Sketch of a setup for visualization using a two-dimensional Talbot interferometer consisting of grating G_1 with period p_1 in the form of a checkerboard and grating G_2 with period p_2 with a grid pattern (*1* — parallel X-ray beam, *2* — object of study, *3* — detector) [118].

It is possible to choose two standard types of two-dimensional gratings: the chessboard type, typically with a duty cycle of 0.5, as shown in Fig. 13, and the mesh type, commonly with a duty cycle of 0.25 [121].

7. Artifact suppression

When all experimental conditions are perfect, images free of artifacts are easy to obtain. However, because of some imperfect experimental settings, the quality of the image can degrade. For example, a polychromatic X-ray beam used in labs can give rise to beam hardening [122–124]. In grating interferometry, the obtained images can also be contaminated by phase wrapping artifacts [125, 126], moiré image artifacts [127–133], and noise artifacts [28, 134] degraded because of the data truncation problem [135, 136].

Beam hardening artifact

When a polychromatic X-ray beam passes through an object, selective attenuation of the flux of lower-energy photons occurs. The effect is conceptually similar to the action of a high-pass filter: only higher-energy photons are present in the transmitted beam, thus increasing the mean energy of the beam (hardening). The consequence of beam hardening is the artificial noise increase in a phase contrast image of strongly absorbing regions of the object [137]. In addition, a false signal appears in the dark-field image, in which only strongly scattering objects and interfaces are usually visible [138]. Additional filtering of the beam can reduce the effect [123, 124].

An experimental calibration procedure, namely the so-called linearization technique, is described in the literature for the correction of radiation hardening [137, 139, 140].

The authors of Ref. [141] extended the monochromatic direct model [142, 143] to the case of polychromatic radiation. The main advantage of the extended model is that the beam hardening artifacts are implicitly damped or even completely removed. The model is used in the iterative reconstruction algorithm, based on maximum likelihood methods [144].

Phase wrapping artifact

The phase periodicity leads to signal overlapping when measuring and transforming the physical quantity of interest, if the initial signal phase exceeds 2π. This effect is known as the phase wrap-around phenomenon. For example, the presence of bone or air cavities in soft tissues leads to a strong phase wrapping that distorts three-dimensional tomographic reconstruction [145, 146]. The existing approaches to correcting or reducing phase wrapping errors in the differential phase data make use of a simultaneously received absorption signal [125, 147]. These approaches are promising, for example, in nondestructive testing, but, because they rely on good absorption contrast, they may fail in biomedical imaging where absorption contrast is weak.

Reference [148] proposes an approach referred to as deconvolution-based multi-order moments analysis (DB-MMA). In contrast to the Fourier component analysis (FCA), DB-MMA naturally avoids the phase wrapping problem by calculating moments of several orders.

The phase wrapping problem can be efficiently solved using the energy dependence $(1/E^2)$ of the phase shift and the measurements at different photon energies with subsequent estimation of the maximum likelihood [149]. The phase shift measurement of the interference pattern at different energies can be performed using a polychromatic X-ray radiation

source in combination with an energy-sensitive detector or using tunable sources of monochromatic X-ray radiation [126].

Moiré artifacts

Moiré artifacts usually occur because of imperfect conditions in the experiment, e.g., inaccurate mechanical displacement of the beam-splitting grating during a phase step or vibration of the experimental setup. In fact, any insignificant change in the grating step violates the agreement between the assumed ideal sinusoidal model of the phase step signal and the obtained data. Because of such disagreement, undesirable image artifacts can appear after extracting the signal by means of the assumed theoretical model of the signal. In addition, the vibration ('judder effect') of the moved grating can lead to misalignment of the interferometer optics [131]. Since the artifacts occurring in this case seem similar to moiré diffraction patterns, they are called moiré artifacts.

Several two-stage algorithms of phase demodulation are known (e.g., [150–153]), using which efficiently decreases the effect of the moiré artifact. However, all two-step algorithms of phase demodulation require preliminary elimination of the interferogram background by a filtering operation [154]. Thus, the interferogram background removal is an important factor for increasing the accuracy of phase determination. Usually, the slowly changing interferogram background can be efficiently removed using a low-frequency filter. However, this filtering method cannot work well when the background intensity exhibits high-frequency variations. References [127, 155–158] describe new methods of fighting artifacts based on the principal component analysis (PCA).

Recently, the deep learning technique [159, 160] attracted enormous research interest because of its remarkable efficiency in multiple applications. The advantages of its power and efficiency make it very interesting to apply the deep learning method to the problem of reducing moiré artifacts in the X-ray interferometric imaging. In particular, the authors of Ref. [133] considered the problem of reducing moiré artifacts as a procedure of image postprocessing using U-net convolutional neural networks (CNNs) [161]. In contrast to common methods of artifact reduction, controlled by algorithms, the efficiency of the CNN-based method of reducing moiré artifacts largely depends on the training data, including both their quality and number.

Obviously, the best way to get rid of moiré artifacts is to abandon the grating movement. For this purpose, it is possible to use the analysis of the moiré Fourier pattern. The visualization system proposed in Ref. [162] is a Talbot–Lau interferometer with a solenoid coil attached to the X-ray tube case. A coil with voltage creates a magnetic field and the resulting Lorentz force acts on the electron beam in the X-ray tube, shifting it with respect to the anode. The misalignment of the phase and absorption gratings creates a rotation moiré pattern. The resulting shift of the focal spot causes an opposite movement of the object projection on the immobile pattern of moiré fringes [163]. In this case, the moiré fringes remain immobile, in spite of the focal spot displacement. As a result, the sample image moves relative to the stationary moiré pattern, efficiently synthesizing the process of sinusoidal variation in the X-ray beam intensity, analogous to the stepwise phase change.

Noise artifact

In interferometry with a unidirectional grating, the phase is usually extracted by one-dimensional direct integration. The integration in the image domain is equivalent to spatial frequency division in the Fourier domain, which acts as a low-pass filter. Therefore, the image is smoothed in the direction of integration. However, in the perpendicular direction, high frequencies are not filtered out and amplify the noise. This leads to strong artifacts in the form of fringes in the image along the direction of integration. As a result, poor quantitative restoration of phase is characterized by a low signal-to-noise ratio, which often complicates the subsequent analysis of the X-ray pattern.

In absorption X-ray imaging, methods of digital filtering are commonly used to reduce the noise [164]. They are simple and efficient for noise suppression, but can blur the image. In the case of fringe artifacts, the noise pattern is inhomogeneous and has a tendency to increase in the direction of linear integration. To suppress such noise, simple digital filtering is inefficient.

One of the artifact correction methods was considered above; it consists in measuring the image in two orthogonal directions using two sets of orthogonal data [114]. The method reduces the fringing artifact, but requires additional alignment of gratings and increases the scanning time and sample radiation dose twofold. Fringe removal by obtaining a two-directional phase gradient was additionally demonstrated using an interferometer with a two-dimensional grating [116]. This approach also requires using a two-dimensional stepped scheme and, thus, quadratically increases the scanning time and radiation dose compared to the unidirectional case.

Therefore, algorithmic methods that require no additional alignments or time consumption are preferable. For example, a method of saving image contrast when reducing the fringe artifact has been proposed [165]. This method is fast and efficient in fighting fringe artifacts at the expense of combining a wavelet transform and Fourier filtering, but it does not remove the residual image noisiness.

The nonlinear conjugate gradient (NLCG) iterative algorithm appeared to be a suitable method for solving the nonlinear optimization problem, although the processing time can rapidly increase for images having very large dimensions [28].

In recent years, various methods of noise removal by means of machine (deep) learning have been applied [166]. Although a method using machine learning requires much time for training, it is more time economical for processing a large amount of data than other methods, since it can be used repeatedly after completing the training. When the noise is uniformly distributed, it can be removed more efficiently by means of machine learning. On the contrary, the fringe artifacts in a phase contrast image are distributed more chaotically, and the machine learning is not as simple as in the case with fixed noise. It is recommended to use a hybrid method, which is a combination of a wavelet transform and machine learning [134].

Data truncation artifact

After obtaining data on the refraction angle, it is possible to perform a tomographic reconstruction of the decrement using the filtered back-projection (FBP) algorithm with the Hilbert filter [17, 167–169].

When using FBP methods, data truncation is a practical problem. This phenomenon is well known in absorption computer tomography. If the detector covers the object image width incompletely, the images reconstructed by FBP will have truncation artifacts. Such artifacts affect differential

phase contrast computed tomography. Due to the small size of diffraction gratings, the scanned field of view (FOV) is often smaller than the size of the studied object. Objects larger than the FOV suffer from data truncation when scanned by such a system. The data truncation problem in differential phase contrast computed tomography (DPC-CT) has been discussed in the literature (see, e.g., [135, 136, 170]).

To suppress the data truncation effect, the authors of Ref. [171] adapted for differential phase contrast tomography the algorithm of projection onto convex sets (POCS) [172–175], used in absorption computed tomography.

8. Tomography

Similar to common radiography, grating interferometry is not restricted to mere X-ray imaging. Three-dimensional information can be obtained by means of computed tomography (CT) both for phase contrast signals [29, 98, 176–181] and for dark field signals [182–187].

During data acquisition for tomographic reconstruction, as an ideal, the sample holder should provide its rotation about the axis normal to the direction of X-ray primary beam propagation, at least through 180°, the final spatial resolution being improved with an increase in the number of projections.

8.1 Optimization of computed tomography methods

However, the FBP method requires a large number of view angles, and, therefore, the time of data acquisition is very large. The long radiation time can also damage biological samples. Therefore, it is relevant to develop algorithms capable of processing a smaller number of views in order to reduce the time of sample exposure to radiation with preservation of a good quality of tomograms. For this purpose, the authors of Ref. [188] used the iterative method of the simultaneous algebraic reconstruction technique (SART) [189]. SART is an algorithm useful in cases where the projection data are limited.

Reference [190] presents a new iteration algorithm of differential phase-contrast visualization, aimed at reducing the number of projections. To solve the reconstruction problem, the algorithm makes use of the variable-direction factor method. Using the algorithm of statistical iterative reconstruction (SIR) [191], the authors of Ref. [192] managed to reduce empirically the number of angular projections from 943 to 211, preserving a sufficient quality of tomograms.

Reference [193] describes a tomographic reconstruction with reduced scan time, combining the methods of total variation (TV) regularization [194] and learning with two dictionaries [195]. The reconstruction uses correlations between the phase and absorption images. Therefore, to restore detailed information about the sample, it is sufficient to have a small number of X-ray projections.

In the phase-stepping method, when performing computed tomography, the procedure of multiple data acquisition is to be repeated for each view angle, which leads to a large number of obtained images, long integral time of data acquisition, and significant dose of sample radiation. Therefore, alongside with the reduction in the number of angular projections, it is often necessary to reduce the number of phase steps.

In direct combination with diffraction phase computed tomography, it is also possible to use back projection methods [67, 196, 197].
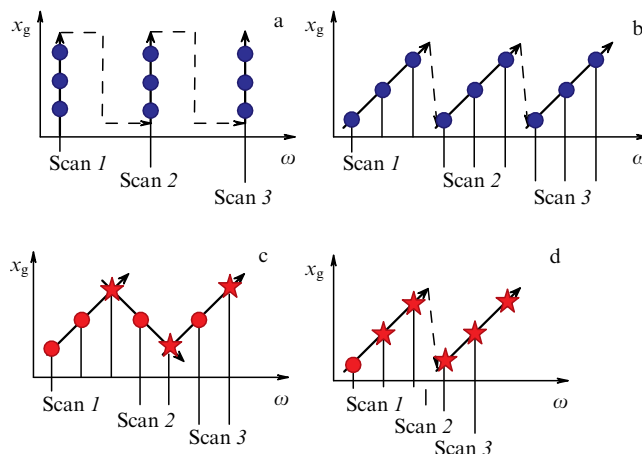

Figure 14. Phase stepping methods presented in the (ω, x_g) coordinate system: (a) standard phase step; (b) interlaced scanning method [179]; (c) SWZ method — one point of each scan is repeatedly used in the next scan; (d) SWI method — all points except one in each scan are repeatedly used in the next scan [200]. Each point or asterisk represents an interferogram recorded by the detector. Interferograms represented by asterisks are used in more than one phase step of scanning.

However, the need to place the data collection point on the slope of the sinusoidal phase curve imposes stringent requirements on grating uniformity and alignment. That is why the back projection method is still restricted to visualization with a small field of view. However, the position of the operating point on the sinusoid slope is not required in the side illumination method [198].

Reference [199] presents a generalized back projection method using side illumination. The generalized method has a potentially wide application field in the case of a large field of view and visualization with a limited radiation dose, for instance, in biomedical applications.

In computed tomography, the scanning of one of the gratings is combined with sample rotation. Every raw interferogram, recorded during this type of tomographic scanning, is recorded in another transverse direction in the x_g position of the grating and/or another angular position ω of the sample. These interferograms can be represented by points in the coordinate system (ω, x_g). Figure 14a shows a standard framework of phase-stepping tomography. All interferograms of one phase scanning are recorded at a fixed angular position of the sample ω, which is rotated only between the subsequent phase scans. The first improvement compared to this scheme, especially taking into account clinical applications of grating interferometry, was the method of interlaced phase stepwise processing [179] (Fig. 14b), in which interferograms of one stepwise scan stroke are recorded at several different angular positions of the sample. This improves the quality of reconstructing the local region of interest (ROI), where otherwise the objects located in the outer region (beyond the detector field of view) would distort the signal in the ROI. In addition, the interlaced scanning method makes the phase-stepping method compatible with a continuous rotation of the sample.

Although the interlaced scanning method is a significant improvement compared to the standard phase-stepping method, it has a general important limitation: the number of interferograms recorded during these tomographic scans should be P times greater than the number N of desirable

projections, i.e., be equal to PN, where $P \geqslant 3$ is the number of steps in the phase-stepping scan.

The sliding window methods described in the present article, i.e., the sliding window zigzag (SWZ) method and the sliding window interlaced (SWI) method, considerably reduce this number. The main idea is that one interferogram can be used to calculate more than one projection, rather than to process the data of a single stepped scan. Even if each scan still contains P interferograms, the actual number of interferograms recorded in the course of full tomography with a sliding window can be much greater than PN.

With the SWZ technique, interferograms are recorded not only when the grating moves in the forward direction but also when it returns to the initial position, as shown in Fig. 14c. In the zigzag method, one of all P interferograms is used when processing two scan strokes, which reduces the effective number of interferograms, recorded per scan stroke, to $P - 1$. Thus, the number of actually recorded interferograms is decreased to $R_{\mathrm{SWZ}} = (P - 1)N + 1$. Since the number of projections N is usually large, $R_{\mathrm{SWZ}} \approx (P - 1)N$. For example, if $P = 3$, then $R_{\mathrm{SWZ}} = 2N$, i.e., the same number of interferograms is recorded as needed in the back projection method.

In the second presented method, SWI (Fig. 14d), the number of interferograms recorded in the process of tomographic scanning can be additionally reduced. The SWI method implies efficient analysis of interlaced phase scans. In fact, if the interferograms are recorded using the interlaced scheme, each group of P sequential interferograms is recorded at P different positions of the grating and, therefore, can form a phase-stepped scan. Thus, $P - 1$ interferograms of each phase scan can be repeatedly used in the processing of the next phase scan, and the number of interferograms necessary for obtaining N projections reduces to a minimum value of $R_{\mathrm{SWI}} = N + P - 1 \approx N$.

Hence, when using the sliding window methods, the same number of final projections is obtained as when using the existing phase schemes, but with a significantly smaller number of interferograms recorded during the scanning and, therefore, with a lower sample radiation dose and shorter data acquisition time. Similarly, at the same radiation dose, sliding window methods provide more accurate angular sampling of final projections, which improves the quality of reconstruction [200].

The image signals in the sliding window methods (absorption, differential phase and dark field) are extracted according to the same algorithm as at the standard phase step [18] based on Fourier analysis, which requires no linearization of the phase-stepping curve.

8.2 Time-resolved computed tomography

The best efficiency of X-ray phase tomography was demonstrated for steady-state objects. But even if it appears possible to reveal the structures of the studied object, their functions may not always be understood. To overcome this limitation, it is necessary to observe the dynamics of the structure, which leads to time-resolved X-ray phase tomography being even more in demand.

Obviously, the most timesaving method of X-ray CT is the method of moiré pattern Fourier transform using a single recording of moiré fringes. Therefore, this method is promising for application in time-resolved X-ray CT [31, 101, 102, 201, 202].

As an example of X-ray grating tomography with a time resolution of 0.5 s, Fig. 15 shows a time series of phase-
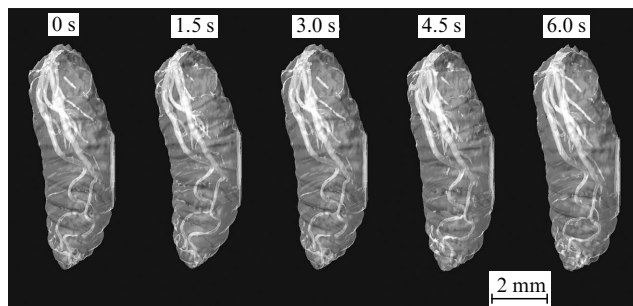

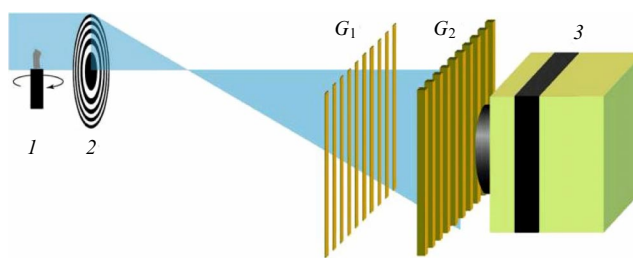**Figure 15.** Frames of a four-dimensional X-ray phase tomogram of a red larva *in vivo* [201].

Figure 16. Schematic diagram of an X-ray full field microscope with a Talbot interferometer (*1* — sample, *2* — Fresnel zone plate, *3* — detector) [206].

contrast images of an alive red larva obtained using polychromatic SR [201].

A disadvantage of the method is the low spatial resolution, limited by the separation between the carrier moiré fringes. To remove this drawback, in Refs [203–207], an X-ray Talbot interferometer was incorporated into an optical configuration of a full field X-ray microscope. In the X-ray range, a Fresnel zone plate (FZP) is commonly used as a focusing element. If a sample is placed before an FZP, it is possible to observe its magnified image. Upon radiation with SR, in the focal plane of the FZP a focus is formed, which is a point source of X-rays for the Talbot interferometer placed before the detector (Fig. 16). Due to microscope magnification, it is possible to achieve a space resolution of 560 nm [207]. Such a microscope was applied to study the postnatal formation of murine bones using the advantage that the degree of mineralization of bones and soft tissues (bone cells and blood vessels) are imaged simultaneously [206, 208]. Using a tomographic microscope to study auditory ossicles of young mice, it was shown that soft tissues, in addition to the bone tissue, could be observed simultaneously without serious radiation damage [207].

In Refs [209, 210], stroboscopic X-ray Talbot interferometry with time resolution was demonstrated to be applicable to quantitative X-ray phase imaging of periodic processes, such as breathing and myocardial contraction in living organisms, or cyclic mechanical tests. To obtain a satisfactory signal-to-noise ratio, the events should repeat multiply with fixed time delays, so that the time resolution does not depend on the rate of data acquisition by the detector. Therefore, the stroboscopic CT can be successfully implemented when using the stepping-phase method.

The authors of Ref. [211] demonstrated time-resolved dark-field visualization of the breathing cycle in mice upon artificial ventilation of the lungs *in vivo*, obtained using a grating interferometer. A time resolution of 0.1 s was

achieved. The stroboscopy was implemented by stepwise displacement of the phase grating, the frequency of scans being matched with the frequency of breathing in the mouse in the experiment.

The limited nature of the photon flux can be compensated for using the stroboscopic technique of multiple 'capture' of the object image in a certain phase of motion. Using polychromatic SR in combination with a high-speed complementary metal oxide semiconductor (CMOS) camera, stroboscopic X-ray Talbot interferometry with a time resolution of 3 μs was realized. By introducing a chopper into a laboratory Talbot–Lau X-ray interferometer, a time resolution of 5 ms was achieved [209].

X-ray phase tomography using a Talbot interferometer and polychromatic SR can provide a three-dimensional video to visualize structural changes in a material consisting of light elements. In Ref. [210], an X-ray stroboscopic phase CT with time resolution using a Talbot interferometer was demonstrated on a vibrating object under a compression-tension fatigue load with a frequency of 24 Hz. Moiré patterns were recorded with an X-ray camera with an exposure of 200 μs, and the phase tomograms were restored at definite phases of vibration.

9. Application

Phase contrast grating interferometry has found wide application in various fields of science and technology [181, 212]. Most publications are devoted to studies in various areas of medicine: mammography [213–219], osteology [178, 220–223], angiology [224–226], nephrology [227, 228], neurosurgery [176, 229]. In many studies, the complementarity of three contrasts (absorption, phase, and dark-field) is also used (see, e.g., [20, 88, 92, 230–237]).

Recently, particular attention of researchers has been attracted to X-ray dark-field grating interferometry.

9.1 Dark-field visualization
Interferometric X-ray dark-field Talbot–Lau visualization was a subject of great interest in the last decade due to its ability to provide characterization of a sample's microstructure beyond the resolution of the image by small-angle scattering effects [18, 238]. Small-angle X-ray scattering allows studying substances of various structures, possessing inhomogeneities of electron density with the size in the range of $1 - 10^3$ nm. The greater the size of a scattering object, the smaller the angular interval in which the scattered radiation is concentrated [239]. Only grating interferometry opened the way to a wide application of dark-field scatter-contrast visualization [18, 240–242].

The centers of X-ray small-angle scattering can be, for instance, pores [243–246], starch granules in sprouting barley seeds [247], or pulmonary tissue alveoli.

Studies in mice *ex vivo* [248, 249] and *in vivo* [92, 211, 250, 251] have shown that healthy pulmonary tissue produces a very strong dark-field signal, generated by small-angle X-ray scattering at multiple air–tissue interfaces, which characterize the microarchitectonics of a normal pulmonary parenchyma. Indeed, in X-ray images of the entire body of a mouse, the lungs are distinguished as the organ that generates the strongest dark-field signal (see Fig. 9c) [92]. Because of the close interrelation between the alveolar structure and the functional condition of lungs, the possibility of obtaining dark-field images of lungs is of primary importance for respiratory medicine and can help us better understand pulmonary diseases. Focal or diffuse lung pathologies modify the pulmonary parenchymatous architecture. This often leads to a decrease in the actually strong dark-field signal from the pulmonary tissue and, hence, lung pathologies can be detected in dark-field X-ray images.

The dark-field diagnostic significance, as compared to absorption visualization, has been demonstrated for various pulmonary diseases, such as pneumothorax [252, 253], emphysema [254, 255], fibrosis [256], bronchopulmonary dysplasia [257], and acute pneumonia [258]. The X-ray dark field contrast is also very suitable for detecting small tumor nodules, which can be missed in a corresponding regular image [259].

At present, lung imaging is probably the most promising medical clinical application of X-ray dark-field visualization [260–262].

Other potential clinical applications of dark-field X-ray imaging include detection of foreign bodies [232, 263], differentiation of kidney stones [264], examination of bone structures [265, 266] and fractures [267], and mammography.

In the diagnosis of multicentric tumor growth, dark-field mammography is superior to standard breast imaging methods, providing better resolution of small calcified tumor nodes and demarcation of breast tumor boundaries [217, 268–273].

The scattering introduced by a sample causes beam expansion and, as a consequence, a decrease in the contrast of interference fringes. The interrelation between the decrease in visibility and characteristics of X-ray small-angle scattering by the sample is well studied [238, 274–276]. The general mathematical description of the dark-field signal in X-ray imaging based on a grating interferometer allows relating the decrease in visibility, caused by the small-angle scattering, to the autocorrelation function $\gamma(\xi)$ [275]:

$$\frac{V_{\text{sca}}(\xi)}{V(\xi)} = \exp\left[-t\sigma(E)(1 - \gamma(\xi))\right], \qquad (22)$$

where V_{sca} and V are the visibility with and without the scattering structures on the beam path, respectively; t is the thickness of the studied object; the total scattering cross-section $\sigma(E)$ determines the scattering probability; and ξ is the correlation length of the grating interferometer, i.e., the length at which the correlation functions inside the sample are measured [277].

In the case of a dilute suspension of monodisperse microspheres, the correlation function $\gamma(\xi)$ is well approximated by the expression [278]

$$\gamma_{\text{sph}}(\xi) \approx \exp\left(-\frac{9q^2}{8}\right), \qquad (23)$$

where the dimensionless parameter $q = \xi/r$ is the ratio of the correlation length to the radius r of the spheres [279].

The dependence of visibility on correlation length shows the selectivity of scattering centers by size: the visibility is better when the correlation length is approximately equal to the radius of the scatterers. Therefore, it is possible to tune the interferometer so that it satisfies this condition and, as a result, distinguish the material containing certain scatterers from a uniform material, even if these materials exhibit the same level of X-ray radiation absorption [184, 242, 274, 280].

The correlation length ξ is determined by the X-ray wavelength λ and the interferometer parameters [238, 274]:

$$\xi = \frac{\lambda L_g}{p_2}, \tag{24}$$

where L_g is the distance between the sample and the analyzer grating G_2. However, this expression is valid for samples placed between the phase grating and analyzer grating. When the sample is placed between the source (grating G_0) and the phase grating G_1 (see Fig. 4), the correlation length is given by the formula [275]

$$\xi = \frac{\lambda d}{p_2}\left(1 - \frac{d_s}{l}\right), \tag{25}$$

where $d_s = l - r$ is the distance between the sample and the phase grating G_1.

By varying the correlation length, it is possible to obtain a complete quantitative characterization of scattering structures having various sizes, shapes, and volume fractions [275, 281].

One dark-field measurement corresponds to one point of the autocorrelation function of the scattering structure, which is not enough to characterize the microstructure. Therefore, to obtain quantitative information about unresolved microstructures in the sample, it is necessary to perform multiple measurements in the range of correlation lengths [276, 282].

In a usual Talbot–Lau interferometer, the correlation length can be changed either by imaging the sample with phase gratings of different periods, which is an impractical and uneconomical solution, or by moving the sample along the optical axis, which in the case of conical beam geometry leads to an undesirable effect of magnification change that hampers further analysis.

If the distance d between the gratings is constant, the dark-field signal $V_{sca}(\xi)/V(\xi)$ in Eqn (22) depends only on the photon energy. It was shown in [279, 283, 284] that it is possible to obtain high-quality X-ray images simultaneously for two different energies of X-ray radiation. Moreover, recently, a so-called two-phase interferometer was proposed [25, 285–287]. When using two phase gratings with small periods, magnified moiré fringes are generated in the detector plane, which can be recorded directly without using an analyzer grating [25]. Moreover, the distance between two phase gratings can be tuned to change the interference period, correspondingly changing the correlation length [288].

In the dark-field visualization, the detector mainly detects the scattered radiation propagating orthogonally to the grating lines [289–291]. Therefore, for highly structured samples, the dark-field signal is an anisotropic quantity. This observation led to the appearance of vector X-ray radiography, a method that allows computing the two-dimensional orientation of a microstructure in the sample using several dark-field images obtained by means of the phase-stepping procedure in various angular positions of the sample, when rotating it about the direction of the beam propagation [292, 293]. In an effort to achieve tomographic reconstruction of this anisotropic signal, anisotropic dark-field X-ray tomography has recently been proposed [294, 295], based on research performed by Malecki et al. [296] and Vogel et al. [297].

Several algorithms were proposed for reconstructing the anisotropic dark field [187, 188, 294, 297–299]. Two-dimensional methods [290, 298] reconstruct the projection of inhomogeneity orientation in one plane. Three-dimensional reconstructions are based on various models. One of the approaches consists of calculating the three-dimensional tensor from two two-dimensional vectors [299], while other approaches imply X-ray tensor tomography [188], constructing a scattering ellipsoid [297], or estimating spherical harmonics [294]. All these methods are based on iterative reconstruction. Schaff et al. [187] proposed a noniterative approach. The authors aligned the gratings perpendicular to the rotation axis so that the sensitivity direction would be parallel to the rotation axis. Thus, the beam projection on the direction of sensitivity is constant during the scan, and standard filtered back-projection (FBP) may be used for two-dimensional reconstruction. Then, the reconstructions of several trajectories are combined [300]. However, all these methods are based on two-dimensional projection models of the three-dimensional structure, i.e., on reconstructing a few two-dimensional sections, and are incompatible with the true three-dimensional trajectories. The authors of Ref. [241] tried to overcome this limitation by proposing a model of dark field projection onto three-dimensional space. This allows direct estimation of the 3D structure and the use of complex 3D trajectories such as a helix.

Currently, fiber-reinforced polymers are widely used in car production and many other industries. Fiber orientation plays a key role in providing mechanical strength to parts. Thanks to scattering anisotropy, the dark-field contrast allows detecting local orientations of fibers in polymers [185, 186, 293, 301–304]. Reference [305] reported the determination of fiber orientation in cardboard, and the authors of Ref. [306] used directional X-ray dark-field visualization to analyze archeological finds. In the process of corrosion, the initial organic-based fabrics vanish as a result of decay, but their structure is largely preserved in the formed mineralized residuals of the fabrics.

Diagnosing and monitoring osteoporosis is a serious problem of common health because of its relation to fragile bone fractures. Osteoporosis is characterized not only by the loss of mineral density of the bone tissue but also by a decrease in bone quality, including the worsening of the trabecular microstructure. For trabecular bone tissue, the correlation was studied between X-ray vector radiography and the trabecular microstructure [260, 292, 296, 307, 308]. As a result, the changes in the trabecular bone structure due to osteoporosis or treatment of osteoporosis can be detected much earlier and with higher sensitivity than with common X-ray methods.

9.2 From laboratory to clinical equipment

From the above, it is clear that the dark-field visualization obtained with grating interferometry can be used for clinical diagnostics and investigation of the dynamics of various diseases.

Since manufacturing diffraction gratings with a large area and large aspect ratio is not a simple problem, the main drawback of X-ray grating interferometry in biomedical studies is the limited field of view.

One of the first X-ray systems of Talbot–Lau phase visualization installed in a hospital (Fig. 17) is described in Refs [221, 309, 310]. It was aimed at diagnosing diseases of the joints, e.g., articular rheumatism, and breast cancer. The visualization of joints is based on the sensitivity of X-ray Talbot–Lau interferometry to cartilage; it was thought that fingers or a palm could be visualized in a field of view of

Figure 17. Talbot–Lau system for X-ray phase visualization installed in a hospital (a) and the obtained absorption image (b) and dark-field image (c) of a part of a palm of the first author of Refs [309, 310].
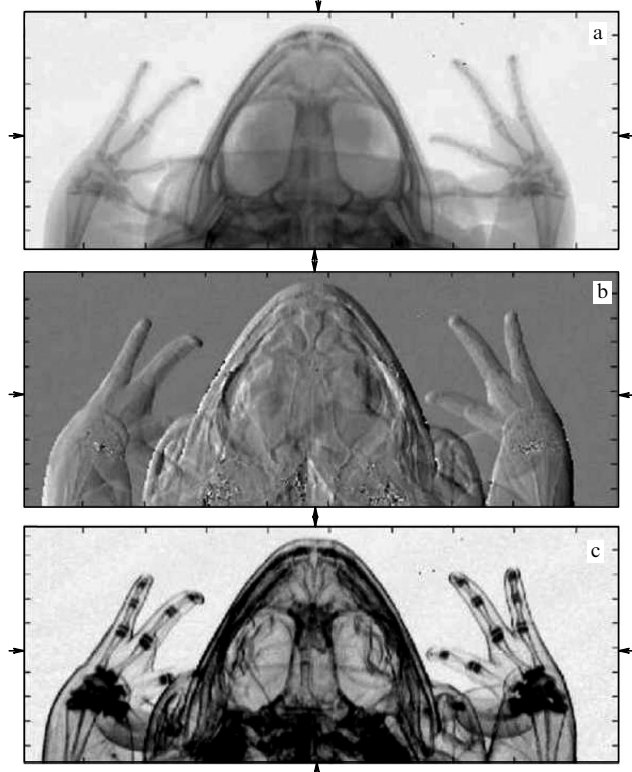

Figure 18. Projection images of a frog obtained by means of four 'joined' analyzer gratings. Absorption-contrast (a), phase-contrast (b), and dark-field (c) images exhibit an insignificant effect of joining. Arrows mark gaps between the gratings (image size is vertically limited because of the limited detector size) [313].

Figure 19. Schematic of a prototype X-ray radiographic chest dark-field scanner. A pig under narcosis is placed on a movable stage *3* and scanned (*1* — X-ray tube, *2* — slit, *4* — detector) [320] (a). Reconstructed absorption image (b) and dark-field image [321] (c) of the whole body of a pig.

case, high-accuracy positioning of an individual grating plate, an active alignment process, an analysis of actual structure position, and plate position correction are necessary to prevent the occurrence of image artifacts.

Figure 18 demonstrates the high potentiality of joining X-ray gratings for a significant increase in the field of view. The authors of Ref. [313] showed that a grating could be cut and joined with required accuracy.

A radical field of view extension can be obtained by the method of slit scanning at the expense of increasing the grating area in one dimension and a scanning procedure in the second dimension. To achieve large fields of view, perpendicular to the scanning direction, several gratings can be joined and aligned in the direction perpendicular to the direction of scanning [253, 314, 315]. Such gratings are called lined. The scanning mode can transform the phase stepping procedure into a one-dimensional shift of the sample [316]. In this connection, Kottler et al. [317] developed a method of slit scanning, in which, by an insignificant change in the distance between the phase and absorption gratings, a dilatation moiré pattern is created with fringes, parallel to the grating lines and equidistantly arranged lines of a single-coordinate detector. Then, the superimposition of interference fringes on the detector lines creates a moiré pattern, similar to the translational moiré pattern in the phase-stepping method. Moving the sample in the direction perpendicular to the orientation of fringes, it is possible to obtain a curve analogous to the phase-stepping sinusoid. The algorithm adapted to the slit-scanning method and used to extract both the absorption signal and the dark-field signal is described in Ref. [318].

The slit-scanning method was successfully applied in dark-field visualization of small animals [319].

Since the thorax anatomy of a pig is very much like that of a human, the thorax X-ray dark-field imaging of the pig's lungs described in [320] and the whole body X-ray radiography of the pig [321] (Fig. 19) can be considered an important milestone in the promotion of the Talbot–Lau interferometer towards its clinical usage.

50×50 mm^2 [311] (Fig. 17b, c). For the second goal, a field of view of 100×100 mm^2 is needed to correspond to the entire breast size.

With a small field of view, the complete image of a studied object can be obtained by visualizing its parts, followed by their joining. For example, the X-ray image of a mouse in Fig. 9 consists of two such segments.

An increase in the field of view can also be obtained by combining several gratings into larger structures [312]. In this
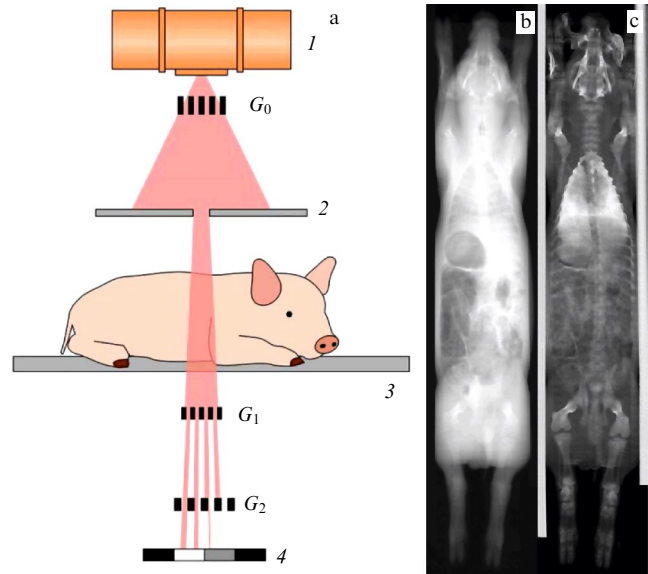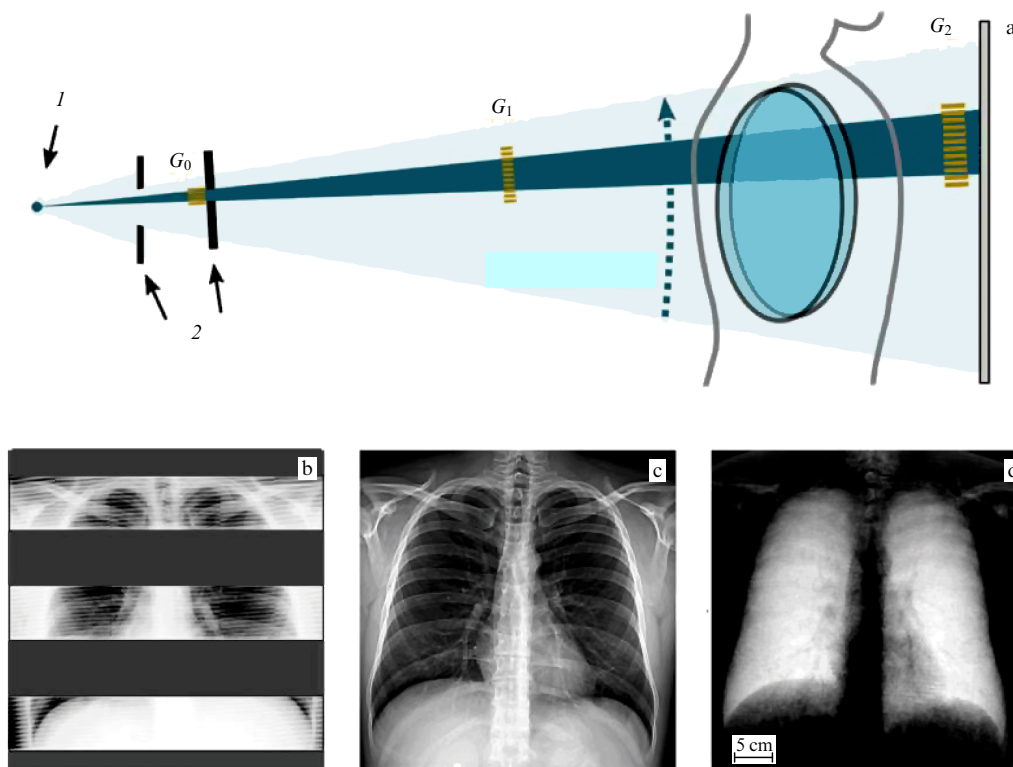
Figure 20. (a) Prototype of an X-ray human chest scanner (*1* — X-ray source, *2* — slits) [323]; (b) examples of raw data of visualization; (c) obtained usual X-ray radiograms and (d) dark-field X-ray radiograms of the chest [261].

However, for some clinical examinations (e.g., in pulmonology [216, 315, 322–325] or mammography [272, 318, 326, 327]), patient movement should be replaced with the X-ray beam scanning. In this case, the radiation source, patient, and detector are immobile, and the gratings of the interferometer are rotated as a whole around the axis, passing through the source focal spot.

To cover the entire chest of a human, in Ref. [261], an interferometer with a prolate grating with an area of about 42×6.5 cm^2 was moved relative to the patient (Fig. 20a), as a result of which the 37×37-cm^2 field of view was obtained. Simultaneously, a plane-plate detector recorded a series of sequential images. Figures 20b, c, d show three (of 195) frames of raw data recorded during one scan of a healthy patient (male, 33 years old, no lung diseases). A moiré pattern superimposed on the patient's thorax image is clearly seen, which is subsequently used to obtain a common absorption radiograph (c) and a dark-field radiograph of the chest (d). The undamaged alveolar structure with a high density of air–tissue interfaces causes strong small-angle scattering, which leads to a strongly expressed dark-field signal in the domain of the lungs. The value of the signal correlates with the number of interfaces [225] and, hence, offers structural information about alveoli, which are commonly below the resolution limit of the imaging system.

For clinical mammography, an interferometric unit was developed and integrated into a modern X-ray slit Philips MicroDose L30 system [272, 318, 326, 327] (Fig. 21). A special method of acquisition and restoration of phase was developed and implemented, which uses the abundance of the collected data inherent in the slit-scanning method. The system operated with a breast up to 5 cm thick with a field of view of 26×21 cm^2. The typical scanning time varied from 10 to
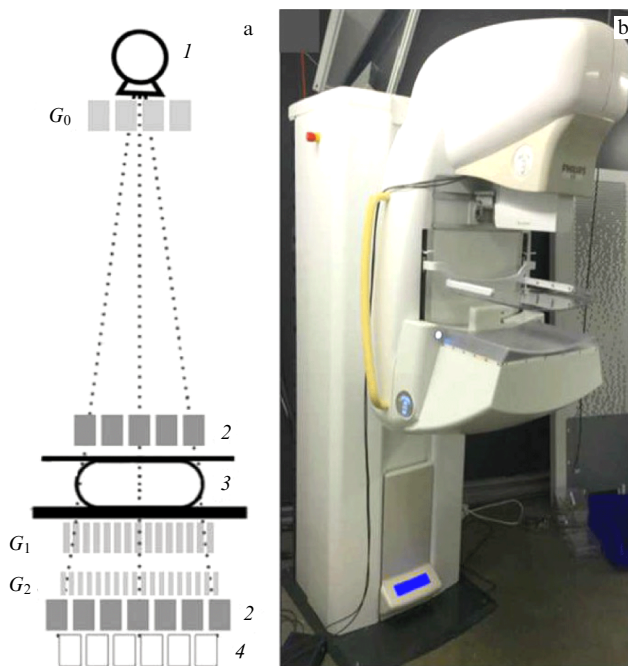

Figure 21. (a) Sketch of a Talbot–Lau interferometer installed in the Philips MicroDose L30 mammography system: *1* — X-ray tube, *2* — collimators, *3* — mammary gland, *4* — detector. (b) External view of the Philips MicroDose L30 system [326].

15 s, and the radiation doses were lower than those typical for usual scanning with identical data acquisition parameters because of the presence of the initial grating G_0. The detector of the system comprised 21 silicon detector lines for photon counting without energy discrimination [328].
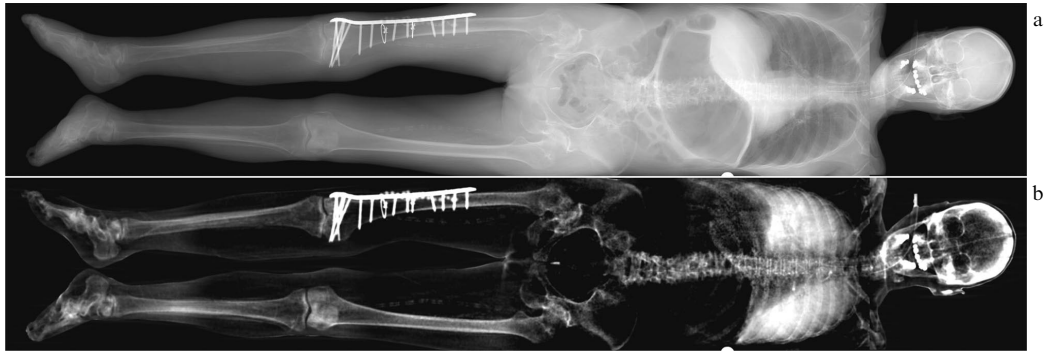
Figure 22. Absorption (a) and dark-field (b) X-ray radiograms of a human corpse without arms in a supine position [329].
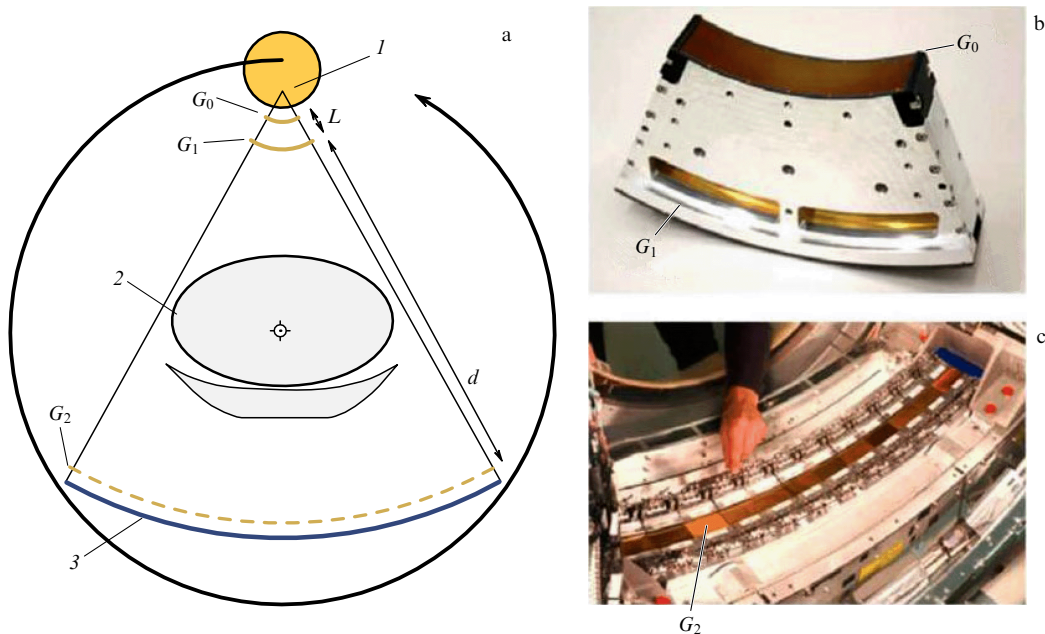

Figure 23. Design of a dark-field clinical computed tomography system. (a) Schematic of a Talbot–Lau interferometer integrated in common medical computed tomography. Inverse geometry of the interferometer allows placing curved gratings G_0 and G_1 close to the source, and grating G_2 close to the detector (*1* — radiation source, *2* — patient, *3* — detector). (b) Special device for bending gratings G_0 and G_1. Rigid mounting is important to ensure the robustness under continuous rotation and large centrifugal forces. (c) In joined grating G_2, the modular adjusting frame is used to position a total of 13 plates [332].

Since, in addition to visualization of the lungs and breast, X-ray imaging of the entire skeleton and the possibility of diagnosing calcification can be of special interest, in Ref. [329] the X-ray visualization of the entire human body was implemented. The images of a dead body (a woman 62 years old, height 162 cm, weight 49 kg) (Fig. 22) were obtained 4 days after her death; the lungs were ventilated by an anesthesia apparatus. These images were formed of six separate scans. The initial grating (G_0) had an area of 5.0×2.5 cm^2, a period of 68.72 µm, and a duty cycle of 0.7. Two other gratings (G_1: period 8.73 µm, duty cycle 0.5; G_2: period 10 µm, duty cycle 0.5) were composed of eight plates, each having a size of 5.0×2.5 cm^2, to make the total grating size of 40×2.5 cm^2. All gratings were mounted on a common frame. The effective field of view of 32×35 cm^2 (in the object plane) was achieved by scanning the frame relative to the object of study.

However, because of the large grating sizes, the systems of slit scanning are particularly sensitive to moiré artifacts occurring due to phase changes caused by the grating vibration. To improve the robustness against these artifacts,

the authors of Ref. [330] extended the reconstruction algorithm by introducing a correction coefficient.

Until recently, the dark-field CT still could not be implemented on an anthropomorphic scale and was restricted to desktop systems for small animals with a scanning duration of a few minutes or more. This was mainly because the adaptation and scaling of the mechanical complexity, rate, and size of a human CT scanner are still an unresolved problem. Substantially increased technological problems are related to the large field of view required for scanning a human, the cylindrical geometry of the interferometer, and the rapidly and continuously rotating gantry. Moreover, the small rotation time (fractions of a second) with all the related vibrational instabilities have set a variety of still unresolved algorithmic problems, which have not been solved at all by means of presently existing desktop systems or systems for small animals with a typical data acquisition time from a few minutes to hours [322, 331].

Reference [332] reported a successful integration of the Talbot–Lau interferometer into a clinical CT gantry and the

results of dark-field CT of an anthropomorphous phantom of a human body.

To maximize the interferometer sensitivity and simultaneously to use the limited space for the gantry, the authors decided to arrange three gratings in an inverse geometry, as shown in Fig. 23a. Curved gratings G_0 and G_1 are placed close to each other and grating G_2 is located at the opposite side of the chamber. This allows efficient use of the space available for the gantry, preserving the initial diameter of 70 cm of the CT chamber for the patient. Distances L and d, as well as the grating characteristics, were optimized in correspondence with the geometry of the particular system and the spectrum of X-ray radiation.

10. Conclusion

In the last two decades, grating Talbot and Talbot–Lau interferometers have begun to be widely used in nondestructive studies in biomedicine, industry, archeology, and food quality inspection. Such popularity among researchers has several explanations. First, grating interferometry allows the simultaneous creation of three complementary X-ray images: absorption, differential-phase, and dark-field. Second, dark-field visualization allows a characterization of objects containing inhomogeneities with a size beyond the limit of the interferometer resolution. Third, the possibility of choosing the shooting geometry, the methods of data acquisition and processing, and the field of view dimensions make grating interferometry an extremely flexible technique. Fourth, a Talbot–Lau interferometer can operate with a common X-ray tube, which allows its use for medical clinical investigations.

These were exactly the prospects of using the X-ray grating interferometry for noninvasive diagnostics of diseases and monitoring their dynamics that have led to the recent creation of several clinical system prototypes. The successful application of the Talbot–Lau interferometer in mammography (the Philips MiscroDose L30 mammographic system) allows us to hope for its clinical application in pulmonology, osteology, and angiology in the nearest future.

References

1. Blokhin M A *Fizika Rentgenovskikh Luchei* (Physics of X-Rays) (Moscow: Gostekhizdat, 1957)
2. Wu X, Dean A, Liu H 'X-ray diagnostic techniques', in *Biomedical Photonics Handbook* (Ed. T VoDinh) (Tampa, FL: CRC Press, 2003) p. 26
3. Fitzgerald R *Phys. Today* **53** (7) 23 (2000)
4. Tao S et al. *Appl. Sci.* **11** 2971 (2021)
5. Bonse U, Hart M *Appl. Phys. Lett.* **6** 155 (1965)
6. Momose A et al. *Nat. Med.* **2** 473 (1996)
7. Snigirev A et al. *Rev. Sci. Instrum.* **66** 5486 (1995)
8. Wilkins S W et al. *Nature* **384** 335 (1996)
9. Ingal V N, Beliaevskaya E A *J. Phys. D* **28** 2314 (1995)
10. Davis T J et al. *Nature* **373** 595 (1995)
11. Morgan K S, Paganin D M, Siu K K W *Appl. Phys. Lett.* **100** 124102 (2012)
12. Momose A et al. *Jpn. J. Appl. Phys.* **42** L866 (2003)
13. Weitkamp T et al. *Opt. Express* **13** 6296 (2005)
14. Momose A *Jpn. J. Appl. Phys.* **44** 6355 (2005)
15. Weitkamp T et al. *Appl. Phys. Lett.* **86** 054101 (2005)
16. Pfeiffer F et al. *Nat. Phys.* **2** 258 (2006)
17. Pfeiffer F et al. *Phys. Rev. Lett.* **98** 108105 (2007)
18. Pfeiffer F et al. *Nat. Mater.* **7** 134 (2008)
19. Zhu P et al. *Proc. Natl. Acad. Sci. USA* **107** 13576 (2010)
20. Pfeiffer F et al. *Z. Med. Phys.* **23** 176 (2013)
21. Talbot H F *Phil. Mag.* **9** 401 (1836)
22. Weitkamp T et al. *Proc. SPIE* **6318** 63180S (2006)
23. Weitkamp T et al. *Proc. SPIE* **5533** 140 (2004)
24. Weitkamp T et al. *Proc. SPIE* **5535** 137 (2004)
25. Miao H et al. *Nat. Phys.* **12** 830 (2016)
26. Miuskov V F, in *Problemy Sovremennoi Kristallografii: Sbornik Pamyati A.V. Shubnikova* (Problems of Modern Crystallography: Collection in Memory of A.V. Shubnikova) (Moscow: Nauka, 1975) p. 186
27. Pinsker Z G, in *Problemy Sovremennoi Kristallografii: Collection in Memory of A.V. Shubnikova* (Problems of Modern Crystallography: Collection in Memory of A.V. Shubnikova) (Moscow: Nauka, 1975) p. 172
28. Thüring T et al. *Opt. Express* **19** 25545 (2011)
29. Momose A et al. *Jpn. J. Appl. Phys.* **45** 5254 (2006)
30. Wang Z et al. *Anal. Bioanal. Chem.* **397** 2137 (2010)
31. Momose A et al. *Opt. Express* **17** 12540 (2009)
32. Myers G R et al. *Phys. Rev. A* **76** 045804 (2007)
33. Thüring T et al. *Appl. Phys. Lett.* **99** 041111 (2011)
34. Pfeiffer F et al. *Nat. Mater.* **7** 134 (2008)
35. Olbinado M P et al. *AIP Conf. Proc.* **1466** 266 (2012)
36. Engelhardt M et al. *Appl. Phys. Lett.* **90** 224101 (2007)
37. Thüring T et al. *AIP Conf. Proc.* **1466** 293 (2012)
38. Thüring T, Stampanoni M *Philos. Trans. R. Soc. A* **372** 20130027 (2014)
39. Birnbacher L et al. *Sci. Rep.* **6** 24022 (2016)
40. Thüring T et al. *Proc. SPIE* **8668** 866813 (2013)
41. Liu X-S et al. *Chinese Phys. B* **19** 040701 (2010)
42. Hipp A et al. *Opt. Express* **22** 30394 (2014)
43. Vila-Comamala J et al. *Microelectron. Eng.* **192** 19 (2018)
44. Romano L et al. *Adv. Eng. Mater.* **22** 2000258 (2020)
45. Vila-Comamala J et al. *Opt. Express* **29** 2049 (2021)
46. Donath T et al. *J. Appl. Phys.* **106** 054703 (2009)
47. Luo R et al. *Rev. Sci. Instrum.* **88** 085102 (2017)
48. Harvey J E, Pfisterer R N *Opt. Eng.* **58** 087105 (2019)
49. Romano L et al. *J. Vac. Sci. Technol. B* **35** 06G302 (2017)
50. Romano L et al. *Microelectron. Eng.* **176** 6 (2017)
51. Kagias M et al. *Mater. Sci. Semicond. Process.* **92** 73 (2019)
52. Momose A et al. *Quantum Beam Sci.* **4** 9 (2020)
53. Gustschin N et al. *Opt. Express* **27** 15943 (2019)
54. Jefimovs K et al. *Micromachines* **12** 517 (2021)
55. Mohr J et al. *AIP Conf. Proc.* **1466** 41 (2012)
56. Meyer P, Schulz J, in *Micromanufacturing Engineering and Technology* (Micro and Nano Technologies, Ed. Y Qin) (Amsterdam: Elsevier, 2015) p. 365
57. Jefimovs K et al. *Proc. SPIE* **10146** 101460L (2017)
58. David C et al. *Microelectron. Eng.* **84** 1172 (2007)
59. Wu B, Kumar A, Pamarthy S *J. Appl. Phys.* **108** 051101 (2010)
60. Romano L, Stampanoni M *Micromachines* **11** 589 (2020)
61. Lei Y et al. *J. Micromech. Microeng.* **24** 015007 (2014)
62. Lei Y et al. *J. Micromech. Microeng.* **26** 065011 (2016)
63. Noda D et al. *Microsyst. Technol.* **14** 1311 (2008)
64. Lynch S K et al. *Proc. SPIE* **8076** 80760F (2011)
65. Lynch S K et al. *J. Micromech. Microeng.* **22** 105007 (2012)
66. Revol V et al. *Nucl. Instrum. Meth. Phys. Res. A* **648** S302 (2011)
67. Wu Z et al. *Med. Phys.* **40** 031911 (2013)
68. Cong W, Xi Y, Wang G, arXiv:1502.01043
69. Lei Y et al. *Nucl. Instrum. Meth. Phys. Res. A* **1004** 165375 (2021)
70. Thüring T et al. *Sci. Rep.* **4** 5198 (2014)
71. Kenntner J et al. *Proc. SPIE* **7804** 780408 (2010)
72. Modregger P et al. *Opt. Express* **19** 18324 (2011)
73. Rieger J et al. *Opt. Express* **24** 13357 (2016)
74. Liu X, Guo J-C, Niu H-B *Chin. Phys. B* **19** 070701 (2010)
75. Rutishauser S et al. *Appl. Phys. Lett.* **98** 171107 (2011)
76. Du Y et al. *Opt. Express* **19** 22669 (2011)
77. Du Y et al. *Phys. Med. Biol.* **61** 8266 (2016)
78. Momose A et al. *Jpn. J. Appl. Phys.* **48** 076512 (2009)
79. Shimura T et al. *Opt. Lett.* **38** 157 (2013)

80. Morimoto N et al. *Opt. Express* **23** 16582 (2015)
81. Zan G et al. *Phys. Med. Biol.* **64** 145011 (2019)
82. Zan G et al. *Proc. Natl. Acad. Sci. USA* **118** e2103126118 (2021)
83. Trimborn B et al. *Phys. Med. Biol.* **61** 527 (2016)
84. Valdivia M P et al. *Appl. Opt.* **57** 138 (2018)
85. Deng K, Li J, Xie W *Opt. Express* **28** 27107 (2020)
86. Wang H et al. *Opt. Express* **19** 16550 (2011)
87. Kayser Y et al. *J. Synchrotron Rad.* **24** 150 (2017)
88. Pfeiffer F et al. *J. Appl. Phys.* **105** 102006 (2009)
89. Revol V et al. *Rev. Sci. Instrum.* **81** 073709 (2010)
90. Li K et al. *Med. Phys.* **41** 011903 (2014)
91. Pfeiffer F et al. *Phys. Rev. Lett.* **94** 164801 (2005)
92. Bech M et al. *Sci. Rep.* **3** 3209 (2013)
93. Wali F et al. *Opt. Eng.* **56** 094110 (2017)
94. Wali F et al. *J. Imaging Sci. Technol.* **64** 20503 (2020)
95. Wang Z L et al. *Chinese Phys. B* **21** 118703 (2012)
96. Li P et al. *Opt. Express* **24** 5829 (2016)
97. Ge Y et al. *Opt. Express* **22** 19268 (2014)
98. Wali F et al. *Imaging Sci. J.* **68** 195 (2020)
99. Fu J et al. *Sci. Rep.* **9** 1113 (2019)
100. Takeda M, Ina H, Kobayashi S *J. Opt. Soc. Am.* **72** 156 (1982)
101. Momose A et al. *Opt. Express* **19** 8423 (2011)
102. Bevins N et al. *Med. Phys.* **39** 424 (2012)
103. Valdivia M P, Stutman D, Finkenthal M *J. Appl. Phys.* **114** 163302 (2013)
104. Valdivia M P, Stutman D, Finkenthal M *Rev. Sci. Instrum.* **85** 073702 (2014)
105. Stutman D, Valdivia M P, Finkenthal M *Appl. Opt.* **54** 5956 (2015)
106. Yuan S et al. *Nucl. Instrum. Meth. Phys. Res. A* **635** S58 (2011)
107. Rutishauser S et al. *Nat. Commun.* **3** 947 (2012)
108. Wang H et al. *Opt. Lett.* **39** 2518 (2014)
109. Wang H et al. *Proc. SPIE* **9206** 920608 (2014)
110. Seaberg M et al. *J. Synchrotron Rad.* **26** 1115 (2019)
111. Zhao S et al. *Proc. SPIE* **11492** 114920Q (2020)
112. Zhao S et al. *Opt. Express* **29** 22704 (2021)
113. Weitkamp T et al. *Proc. SPIE* **5533** 140 (2004)
114. Kottler C et al. *Opt. Express* **15** 1175 (2007)
115. Scherer K et al. *PLoS ONE* **10** e0130776 (2015)
116. Zanette I et al. *Phys. Rev. Lett.* **105** 248102 (2010)
117. Zanette I et al. *AIP Conf. Proc.* **1466** 12 (2012)
118. Rutishauser S et al. *Microelectron. Eng.* **101** 12 (2013)
119. Itoh H et al. *Opt. Express* **19** 3339 (2011)
120. Zanette I et al. *AIP Conf. Proc.* **1221** 73 (2010)
121. Tao S et al. *Front. Phys.* **9** 672207 (2021)
122. Bevins N et al. *Proc. SPIE* **7961** 7961H (2011)
123. Bevins N et al. *Proc. SPIE* **8668** 866816 (2013)
124. Yan A, Wu X, Liu H *Opt. Express* **25** 24690 (2017)
125. Jerjen I et al. *Opt. Express* **19** 13604 (2011)
126. Epple F M et al. *Opt. Express* **21** 29101 (2013)
127. Seifert M et al. *Phys. Med. Biol.* **61** 6441 (2016)
128. Kaeppler S et al. *J. Med. Imag.* **4** 034005 (2017)
129. Hauke C et al. *Opt. Express* **25** 32897 (2017)
130. Hauke C et al. *Phys. Med. Biol.* **63** 135018 (2018)
131. Dittmann J et al. *J. Imaging* **4** 77 (2018)
132. De Marco F et al. *Opt. Express* **26** 12707 (2018)
133. Chen J et al. *Phys. Med. Biol.* **64** 195013 (2019)
134. Kim M et al. *J. Korean Soc. Radiol.* **14** 937 (2020)
135. Pfeiffer F et al. *Phys. Rev. Lett.* **101** 168101 (2008)
136. Köhler T, Noo F *Phys. Rev. Lett.* **102** 039801 (2009)
137. Chabior M et al. *Med. Phys.* **38** 1189 (2011)
138. Kaeppler S et al. *Med. Image Comput. Comput. Assist. Interv.* **17** (1) 170 (2014)
139. Munro P, Olivo A *Phys. Rev. A* **87** 053838 (2013)
140. Engelhardt M et al. *J. Microsc.* **232** 145 (2008)
141. Schiffers F et al. *Proc. Fully 3D'* **17** 249 (2017)
142. Brendel B et al. *Med. Phys.* **43** 188 (2016)
143. Ritter A, Anton G, Weber T *PLoS ONE* **11** e0163016 (2016)
144. Elbakri I, Fessler J *IEEE Trans. Med. Imaging* **21** 89 (2002)
145. Zanette I et al. *Phys. Status Solidi A* **208** 2526 (2011)
146. Li K et al. *AIP Conf. Proc.* **1466** 175 (2012)
147. Haas W et al. *Proc. SPIE* **7962** 79624R (2011)
148. Wu C et al. *Med. Phys.* **47** 1189 (2020)
149. Pascazio V, Schirinzi G *IEEE Trans. Image Process* **11** 1478 (2002)
150. Kreis T M, Juptner W P O *Proc. SPIE* **1553** 263 (1992)
151. Vargas J et al. *Opt. Lett.* **36** 3485 (2011)
152. Vargas J et al. *Opt. Lett.* **37** 443 (2012)
153. Deng J et al. *Opt. Lett.* **37** 4669 (2012)
154. Quiroga J A, Servin M *Opt. Commun.* **224** 221 (2003)
155. Vargas J, Quiroga J A, Belenguer T *Opt. Lett.* **36** 1326 (2011)
156. Vargas J, Sorzano C *Opt. Lasers Eng.* **51** 637 (2013)
157. Vargas J, Carazo J, Sorzano C *Appl. Phys. B* **115** 355 (2014)
158. Deng J et al. *Opt. Express* **23** 12222 (2015)
159. LeCun Y, Bengio Y, Hinton G *Nature* **521** 436 (2015)
160. Wang G, Ye J C, De Man B *Nat. Mach. Intell.* **2** 737 (2020)
161. Ronneberger O, Fischer P, Brox T, arXiv:1505.04597
162. Miao H et al. *Proc. Natl. Acad. Sci. USA* **110** 19268 (2013)
163. Wen H et al. *PLoS ONE* **8** e78276 (2013)
164. Zhu Y, Huang C *Phys. Proced.* **25** 609 (2012)
165. Munch B, Trtik P, Marone F *Opt. Express* **17** 8567 (2009)
166. He Z et al. *Appl. Opt.* **57** 155 (2018)
167. Pfeiffer F et al. *Nucl. Instrum. Meth. Phys. Res. A* **580** 925 (2007)
168. Qi Z, Chen G-H *Phys. Med. Biol.* **52** N417 (2007)
169. Chen G, Qi Z *Phys. Med. Biol.* **53** 1015 (2008)
170. Anastasio M A, Pan X *Opt. Lett.* **32** 3167 (2007)
171. Lauzier P T et al. *Phys. Med. Biol.* **57** N117 (2012)
172. Defrise M et al. *Inverse Problems* **22** 1037 (2006)
173. Ye Y et al. *Int. J. Biomed. Imaging* **2007** 63634 (2007)
174. Kudo H et al. *Phys. Med. Biol.* **53** 2207 (2008)
175. Courdurier M et al. *Inverse Problems* **24** 065001 (2008)
176. Pfeiffer F et al. *Phys. Med. Biol.* **52** 6923 (2007)
177. Herzen J et al. *PLoS ONE* **9** e83369 (2014)
178. Herzen J et al. *PLoS ONE* **14** e0212106 (2019)
179. Zanette I et al. *Appl. Phys. Lett.* **98** 094101 (2011)
180. Takashima K et al. *J. Synchrotron Rad.* **22** 136 (2015)
181. Birnbacher L et al. *Eur. J. Nucl. Med. Mol. Imaging* **48** 4171 (2021)
182. Wang Z-T et al. *Appl. Phys. Lett.* **95** 094105 (2009)
183. Bech M et al. *Phys. Med. Biol.* **55** 5529 (2010)
184. Revol V et al. *J. Appl. Phys.* **110** 044912 (2011)
185. Lauridsen T, Lauridsen E M, Feidenhans'l R *Appl. Phys. A* **115** 741 (2014)
186. Hannesschlägera C et al. *Case Stud. Nondestruct. Test. Eval.* **3** 34 (2015)
187. Schaff F et al. *Sci. Rep.* **7** 3307 (2017)
188. Malecki A et al. *Europhys. Lett.* **105** 38002 (2014)
189. Andersen A H, Kak A C *Ultrason. Imaging* **6** 81 (1984)
190. Nilchian M et al. *Opt. Express* **21** 5511 (2013)
191. Hahn D et al. *Sci. Rep.* **5** 10452 (2015)
192. Umkehrer S et al. *Rev. Sci. Instrum.* **90** 103103 (2019)
193. Bai H et al. *Opt. Express* **26** 26566 (2018)
194. Chen G-H, Tang J, Leng S *Med. Phys.* **35** 660 (2008)
195. Lu Y, Zhao J, Wang G *Phys. Med. Biol.* **57** 173 (2012)
196. Diemoz P C et al. *Opt. Express* **19** 1691 (2011)
197. Marschner M et al. *PLoS ONE* **12** e0184217 (2017)
198. Hagen C K et al. *J. Phys. D* **49** 255501 (2016)
199. Wu Z et al. *J. Synchrotron Rad.* **28** 854 (2021)
200. Zanette I et al. *Proc. Natl. Acad. Sci. USA* **109** 10199 (2012)
201. Momose A, Yashiro W *AIP Conf. Proc.* **1236** 195 (2010)
202. Yashiro W, Noda D, Kajiwara K *Appl. Phys. Express* **10** 052501 (2017)
203. Takeda Y et al. *Appl. Phys. Express* **1** 117002 (2008)
204. Momose A et al. *J. Phys. Conf. Ser.* **186** 012044 (2009)
205. Berujon S et al. *Opt. Lett.* **37** 1622 (2012)
206. Nango N et al. *Opt. Express* **4** 917 (2013)
207. Takano H et al. *AIP Adv.* **10** 095115 (2020)
208. Nango N et al. *Bone* **84** 279 (2016)
209. Olbinado M P et al. *Appl. Phys. Express* **6** 096601 (2013)
210. Wu Y, Takano H, Momose A *Rev. Sci. Instrum.* **92** 043702 (2021)
211. Gradl R et al. *IEEE Trans. Image Process.* **38** 649 (2019)
212. Kastner J et al. *Test Cond. Monit.* **61** 149 (2019)
213. Stampanoni M et al. *Invest. Radiol.* **46** 801 (2011)
214. Wang Z et al. *J. Instrum.* **8** C07011 (2013)
215. Wang Z et al. *Nat. Commun.* **5** 3797 (2014)
216. Roessl E et al. *Philos. Trans. R. Soc. A* **372** 20130033 (2014)
217. Hauser N et al. *Invest. Radiol.* **49** 131 (2014)
218. Willner M et al. *Phys. Med. Biol.* **59** 1557 (2014)
219. Hellerhoff K et al. *PLoS ONE* **14** e0210291 (2019)

220. Stutman D et al. *Phys. Med. Biol.* **56** 5697 (2011)
221. Tanaka J et al. *Z. Med. Phys.* **23** 222 (2013)
222. Nagashima M et al. *Anat. Sci. Int.* **89** 95 (2014)
223. Khimchenko A et al. *APL Bioeng.* **2** 016106 (2018)
224. Hetterich H et al. *Radiology* **271** 870 (2014)
225. Hetterich H et al. *Invest. Radiol.* **50** 686 (2015)
226. Notohamiprodjo S et al. *Invest. Radiol.* **53** 26 (2018)
227. Velroyen A et al. *PLoS ONE* **9** e109562 (2014)
228. Braunagel M et al. *Sci. Rep.* **7** 45400 (2017)
229. Schulz G et al. *J. R. Soc. Interface* **7** 1665 (2010)
230. Uehara M et al. *J. Appl. Phys.* **114** 134901 (2013)
231. Sarapata A et al. *Appl. Phys. Lett.* **106** 154102 (2015)
232. Einarsdottir H et al. *Food Control* **67** 39 (2016)
233. Revol V, Hanser C, Krzemnicki M *Case Stud. Nondestruct. Test. Eval.* **6** 1 (2016)
234. Gresil M et al. *Appl. Compos. Mater.* **24** 513 (2017)
235. Wang S X et al. *Nucl. Sci. Tech.* **28** 24 (2017)
236. Lau S H et al., in *Proc. of the ISTFA 2020. ISTFA 2020: Papers Accepted for the Planned 46th Intern. Symp. for Testing and Failure Analysis*, p. 79, paper No. istfa2020p0079, https://doi.org/10.31399/asm.cp.istfa2020p0079
237. Pathak A K et al. *Composite Structures* **253** 112758 (2020)
238. Yashiro W et al. *Opt. Express* **18** 16890 (2010)
239. Svergun D I, Feigin L A *Structure Analysis by Small-Angle X-Ray and Neutron Scattering* (New York: Plenum Press, 1987); Translated from Russian: *Rentgenovskoe i Neitronnoe Malouglovoe Rasseyanie* (Moscow: Nauka, 1986)
240. Gusenbauer C et al. *Case Stud. Nondestruct. Test. Eval.* **6** 30 (2016)
241. Felsner L et al. *Sci. Rep.* **9** 9216 (2019)
242. Graetz J et al. *Phys. Med. Biol.* **65** 235017 (2020)
243. Yang F et al. *Appl. Phys. Lett.* **105** 154105 (2014)
244. Prade F et al. *Cement Concrete Res.* **74** 19 (2015)
245. Prade F et al. *Sci. Rep.* **6** 29108 (2016)
246. Yang F et al. *Mater. Charact.* **142** 560 (2018)
247. Nielsen M S et al. *J. Food Eng.* **198** 98 (2017)
248. Schleede S et al. *Proc. Natl. Acad. Sci. USA* **109** 17880 (2012)
249. Schwab F et al. *Z. Med. Phys.* **23** 236 (2013)
250. Yaroshenko A et al. *Sci. Rep.* **5** 17492 (2015)
251. Burkhardt R et al. *Phys. Imaging Radiat. Oncol.* **20** 11 (2021)
252. Hellbach K et al. *Invest. Radiol.* **51** 597 (2016)
253. Hellbach K et al. *Sci. Rep.* **8** 2602 (2018)
254. Meinel F G et al. *Invest. Radiol.* **49** 653 (2014)
255. Hellbach K et al. *Invest. Radiol.* **50** 430 (2015)
256. Hellbach K et al. *Sci. Rep.* **7** 340 (2017)
257. Yaroshenko A et al. *Sci. Rep.* **6** 24269 (2016)
258. Hellbach K et al. *Sci. Rep.* **8** 2096 (2018)
259. Scherer K et al. *Sci. Rep.* **7** 402 (2017)
260. Willer K et al. *PLoS ONE* **13** e0204565 (2018)
261. Willer K et al. *Lancet Digit. Health* **3** e733 (2021)
262. Zimmermann G S et al. *Eur. Radiol. Exp.* **6** 9 (2022)
263. Braig E-M et al. *Eur. Radiol. Exp.* **2** 1 (2018)
264. Scherer K et al. *Sci. Rep.* **5** 9527 (2015)
265. Wen H et al. *Radiology* **251** 910 (2009)
266. Jud C et al. *Sci. Rep.* **7** 14477 (2017)
267. Hauke C et al. *Proc. SPIE* **10573** 105734F (2018)
268. Anton G et al. *Z. Med. Phys.* **23** 228 (2013)
269. Michel T et al. *Phys. Med. Biol.* **58** 2713 (2013)
270. Grandl S et al. *Eur. Radiol.* **25** 3659 (2015)
271. Scherer K et al. *Sci. Rep.* **6** 36991 (2016)
272. Arboleda C et al. *Opt. Express* **25** 6349 (2017)
273. Emons J et al. *Ther. Adv. Med. Oncol.* **12** (2020) https://doi.org/10.1177/1758835920957932
274. Lynch S K et al. *Appl. Opt.* **50** 4310 (2011)
275. Strobl M *Sci. Rep.* **4** 7243 (2016)
276. Gkoumas S et al. *Sci. Rep.* **6** 35259 (2016)
277. Prade F et al. *Europhys. Lett.* **112** 68002 (2015)
278. Andersson R et al. *J. Appl. Cryst.* **41** 868 (2008)
279. Sellerer T et al. *IEEE Trans. Med. Imag.* **40** 974 (2021)
280. Blykers B K et al. *Sci. Rep.* **11** 18446 (2021)
281. Strobl M et al. *J. Appl. Cryst.* **49** 569 (2016)
282. Harti R P et al. *Sci. Rep.* **7** 44588 (2017)
283. Kottler C et al. *J. Appl. Phys.* **108** 114906 (2010)
284. Wang S et al. *Opt. Eng.* **58** 114105 (2019)
285. Kagias M et al. *Appl. Phys. Lett.* **110** 014105 (2017)
286. Yan A, Wu X, Liu H *Opt. Express* **27** 22727 (2019)
287. Yan A, Wu X, Liu H *J. X-ray Sci. Technol.* **28** 1055 (2020)
288. Pandeshwar A et al. *Opt. Express* **28** 19187 (2020)
289. Jensen T H et al. *Phys. Rev. B* **82** 214103 (2010)
290. Revol V et al. *J. Appl. Phys.* **112** 114903 (2012)
291. Bayer F et al. *Opt. Express* **21** 019922 (2013)
292. Potdevin G et al. *Phys. Med. Biol.* **57** 3451 (2012)
293. Prade F et al. *NDT E Int.* **86** 65 (2017)
294. Wieczorek M et al. *Phys. Rev. Lett.* **117** 158101 (2016)
295. Wieczorek M et al. *Sci. Rep.* **8** 14345 (2018)
296. Malecki A et al. *PLoS ONE* **8** e61268 (2013)
297. Vogel J et al. *Opt. Express* **23** 15134 (2015)
298. Bayer F L et al. *Proc. Natl. Acad. Sci. USA* **111** 12699 (2014)
299. Hu S et al., in *Bildverarbeitung für die Medizin* (Eds H Handels, T Deserno, H P Meinzer, T Tolxdorff) (Berlin: Springer Vieweg, 2015) p. 492
300. Felsner L et al., in *Bildverarbeitung für die Medizin* (Eds H Handels et al.) (Wiesbaden: Springer Vieweg, 2019) p. 264
301. Revol V et al. *NDT E Int.* **58** 64 (2013)
302. Plank B et al. *Mater. Sci. Forum* **825** 868 (2015)
303. Glinz J et al. *J. Mater. Sci.* **56** 9712 (2021)
304. Kasai Y et al. *Adv. Compos. Mater.* **30** 591 (2021)
305. Reza S et al. *JINST* **9** C04032 (2014)
306. Ludwig V et al. *J. Imaging* **4** 58 (2018)
307. Schaff F et al. *Sci. Rep.* **4** 3695 (2014)
308. Scholz J et al. *Sci. Rep.* **11** 19021 (2021)
309. Momose A et al. *Philos. Trans. R. Soc. A* **372** 20130023 (2014)
310. Momose A *Phys. Med.* **79** 93 (2020)
311. Noda D et al. *J. Solid Mech. Mater. Eng.* **3** 416 (2009)
312. Schröter T J et al. *Rev. Sci. Instrum.* **88** 015104 (2017)
313. Meiser J et al. *J. X-ray Sci. Technol.* **24** 379 (2016)
314. Fingerle A A et al. *Eur. Radiol. Exp.* **3** 25 (2019)
315. Andrejewski J et al. *Sci. Rep.* **11** 23504 (2021)
316. Roessl E et al. *Proc. SPIE* **9033** 90330C (2014)
317. Kottler C et al. *Rev. Sci. Instrum.* **78** 043710 (2007)
318. Köhler T et al. *Med. Phys.* **42** 1959 (2015)
319. Bachche S et al. *Sci. Rep.* **7** 6711 (2017)
320. Gromann L B et al. *Sci. Rep.* **7** 4807 (2017)
321. Hauke C et al. *Med. Phys.* **45** 2565 (2018)
322. Horn F et al. *Sci. Rep.* **8** 2325 (2018)
323. Gassert F T et al. *Radiology* **301** 389 (2021)
324. Willer K et al. *PLoS ONE* **13** e0204565 (2018)
325. Patera A et al. *J. Phys. D* **55** 045103 (2022)
326. Lång K et al. *Eur. Radiol. Exp.* **3** 19 (2019)
327. Arboleda C et al. *Eur. Radiol.* **30** 1419 (2020)
328. Aslund M et al. *Med. Phys.* **34** 1918 (2007)
329. Andrejewski J et al. *Eur. Radiol. Exp.* **5** 6 (2021)
330. Seifert M et al. *Sci. Rep.* **9** 4199 (2019)
331. Velroyen A et al. *EBioMedicine* **2** 1500 (2015)
332. Viermetz M et al. *Proc. Natl. Acad. Sci. USA* **119** e2118799119 (2022)